

Wide-ranged multiphase equation of state for iron and model variations addressing uncertainties in high-pressure melting

Christine J. Wu,^{*} Lorin X. Benedict,[†] Philip C. Myint[‡],[‡] Sebastien Hamel, Carrie J. Prisbrey[Ⓧ], and James R. Leek[Ⓧ]
Lawrence Livermore National Laboratory, Livermore, California 94550, USA

 (Received 9 September 2022; revised 29 March 2023; accepted 15 May 2023; published 7 July 2023)

We describe the construction of a wide-ranged multiphase equation of state for elemental iron, consisting of four solid phases and one fluid phase. The free-energy models for the phases are constrained by fitting to a broad swath of ambient, static, and dynamic high-pressure experimental data, including recent ramp-compression and shock-ramp recrystallization experiments. In order to better describe the conditions near Earth's inner-core boundary, *ab initio* electronic-structure calculations of various types have been carried out for the hcp and liquid phases and used as additional constraints. Given the variability of reported iron melting temperatures in the 1–3 Mbar range, we construct EOS model variations based on two separate $T_{\text{melt}}(P)$ curves: lower- T_{melt} and higher- T_{melt} . Our analysis shows that only the higher- $T_{\text{melt}}(P)$ data are consistent with reported shock-melting pressure measurements. Furthermore, our examination of the recrystallization data from a recent shock-ramp x-ray diffraction study motivates a family of EOS models that address experimental uncertainties and provide a range of possible $T_{\text{melt}}(P)$ curves that have a somewhat lower melt temperature above 5 Mbar than the one reported in that study. This family of multiphase EOS models allow us to suggest new experiments to further reduce the uncertainties on the high-pressure melt curve, and they should also enable more accurate predictions of complex high- P , T processes involving iron. We show their potential utility by applying these EOSs to the investigation of properties of interest to planetary science, such as the vaporization entropy, critical temperature and density, Earth inner-core boundary temperature plus inner- and outer-core density deficits.

DOI: [10.1103/PhysRevB.108.014102](https://doi.org/10.1103/PhysRevB.108.014102)

I. INTRODUCTION

Elemental iron (Fe) is one of the most studied materials in high-pressure science, a result of its importance in understanding the interior structure of Earth-sized and super-Earth planets. Experimental investigations have involved all manner of ambient-pressure [1–4], static-compression (e.g., diamond-anvil cell [DAC]) [5–38], and dynamic-compression (shock Hugoniot or ramp compression) [5,39–85] measurements conducted over the past seven decades, leading to a picture of the Fe phase diagram up to (at least) several Mbar for the five known phases of Fe: α (body-centered cubic [bcc]), ϵ (hexagonal closed-packed [hcp]), γ (face-centered cubic [fcc]), δ (bcc; higher T than α), and the liquid. This expansive set of data includes detailed information on isobars, pressure isotherms (in the form of density as a function of pressure and temperature), and shock Hugoniot. Many of these studies make explicit reference to planetary-science applications, and more particularly to the greater understanding of the nature

of Earth's core [5–14,38–42,85–108]. Here, recurring themes include addressing which solid phases are likely to be present in certain regions within Earth (since different phases are expected to transmit seismic waves differently), and discovering precise values for the pressure-dependent melt temperature $T_{\text{melt}}(P)$ in multi-Mbar conditions, needed for modeling the long-time evolution of the geodynamo in Earth and Earth-like planets.

Most of the experimental work to infer $T_{\text{melt}}(P)$ for Fe over the past four decades has involved DAC studies and measurements of shock melting, although it is only in the former experiments where the temperature T is actually controlled. This set of DAC and shock data includes the work of Yoo *et al.* [7,67], Saxena *et al.* [19], Boehler *et al.* [18,26], Nguyen and Holmes [71], Anzellini *et al.* [29], Ping *et al.* [75], and Sinmyo *et al.* [14], among others. In general, the reported values of the melt temperature $T_{\text{melt}}(P)$ for pressures $0.5 \text{ Mbar} < P < 2.7 \text{ Mbar}$ fall into two categories: higher- T_{melt} values [29,85], and lower- T_{melt} values [14,26]. It is still a point of contention as to which set of inferences is more correct. As a result, earlier reports show the predicted temperatures of iron at the inner-core boundary (ICB, e.g., extrapolation to 3.3 Mbar) to vary substantially between about 4000 to 8000 K. Likewise, there is a long-standing controversy surrounding the presence or absence of a high-pressure ($> 1 \text{ Mbar}$) stable bcc phase out of which melting occurs; many experiments suggest high- P melting out of hcp (see, e.g., [24,29,34,85]), while others (along with differing interpretations of the former set of experiments, motivated in part by simulations) suggest

^{*}Corresponding author: wu5@llnl.gov

[†]Corresponding author: benedict5@llnl.gov

[‡]Corresponding author: myint1@llnl.gov

melting out of a high- P , T bcc phase [37,38,103–111]. The debate on the core structure is further complicated by the uncertainty associated with its composition, which is thought to consist of $\sim 90\%$ iron, supplemented by other elements, such as Ni, S, Si, O, C, H, Au [112]. The presence of these other components can change the relative phase stability of hcp and bcc. Indeed, for *pure* Fe, so far only the hcp phase has been observed experimentally under both static and dynamic compression up to and exceeding the ICB conditions. In contrast, a high-pressure bcc phase was reported for a Fe–Ni alloy under static compression [38]. Nevertheless, the behavior of pure Fe at Earth-core conditions provides a critical baseline and constraint for the modeling of planetary evolution and geodynamics.

The persistent disagreements about the Fe phase diagram illustrate that high- P Fe remains an active area of experimental research. Not surprisingly, therefore, many theorists have used their tools to predict the high- P Fe phase diagram from first-principles quantum simulations [90,91,105–111,113–129]. While the lower- P regime for Fe is complicated by the propensity for magnetic moment formation and ordering, it is believed that properties of Fe at multi-Mbar pressures are free from these complexities, and it is widely assumed that fairly straightforward applications of density functional theory (DFT) and DFT-based molecular dynamics (DFT–MD) should yield accurate results, provided that the phases in question are simulated with the requisite statistical and numerical fidelity at elevated temperatures (which is not necessarily easy to achieve, especially for melting calculations). Tethered to the prediction of relative phase stability is the construction of a multiphase equation of state (EOS) of Fe that is self-consistent with the phase diagram. And indeed, the modeling needs of planetary scientists in particular require an accurate multiphase Fe EOS for many of their most pressing problems, including ICB conditions needed to infer the age of the core, the density deficit for core composition, and potential core vaporization resulting from giant impacts. The creation and dissemination of such an EOS for *pure* Fe is the subject of this paper.

There have been many attempts to construct accurate Fe EOS models over the years. Notable recent efforts in this regard fall into two general categories: (1) those which put forth *narrow-ranged* Fe EOS models, meant to be valid over restricted ranges of compression and temperature, and (2) those which propose *wide-ranged* Fe EOS models that are at least sensible over many decades of density ρ and T . Examples of narrow-ranged multiphase Fe EOS models include those of Boettger and Wallace [130] concentrating on the $\alpha \rightarrow \epsilon$ transition at 0.13 Mbar (constructed in the context of a study of phase metastability and kinetics for this transition), the Tsujino *et al.* EOS for the γ phase [131], and the work of Dyachkov *et al.* [132]. Wide-ranged Fe EOS models include the works of Kerley [133] and Medvedev [134], each of which make use of a combination of theoretical and (primarily) experimental constraints, employing semi-empirical free-energy models similar in spirit to those of the aforementioned narrow-ranged studies. Also in this category is the recent multiphase EOS of Sjöström and Crockett [135], in which a combination of Kohn–Sham DFT–MD and orbital-free DFT–MD calculations were performed to provide most of the constraints

for the model. Sjöström and Crockett rely on the Boettger–Wallace limited-range EOS for their α and ϵ phases, and they use experimental data on γ , δ , and the liquid to constrain the low-pressure part of their EOS. DFT–MD is used as the primary constraint for most of the rest of their wide-ranged model, together with interpolation schemes to connect high- and low-pressure regions. In our paper, we take experimental data as our primary source of constraint. However, we also generate new first-principles DFT results for the hcp solid and liquid for conditions pertaining to the ICB, and use them for both secondary constraints and model validation.

Because the Kerley (1993) [133] and Medvedev (2014) [134] EOS models are semi-empirical and were fit primarily to experimental data, they are each in good accord with most of the static and dynamic high-pressure data available at the times of their construction. However, since the experimental picture of Fe at high pressure is ever evolving, aspects of these EOSs are less up-to-date, presently. For example, the Kerley EOS has a $T_{\text{melt}}(P)$ that is somewhat off at high- P from both the recent higher- T_{melt} [29,85] and lower- T_{melt} [14] inferences, and its phase diagram possesses a thermodynamically stable γ phase even at 100-Mbar pressures, far above the reported stability of γ , in contradiction to experiment and *ab initio* calculations. The Medvedev EOS, on the other hand, is in far better agreement with the most recent data, given that it was constructed later. But as any *single* EOS must, it chooses just a particular set of $T_{\text{melt}}(P)$ inferences [30] as a constraint, thereby discounting alternate estimations (e.g., those from Boehler *et al.* [26] and the more recent Sinmyo *et al.* [14]). The Sjöström–Crockett EOS (published in 2018) is in notable disagreement with much of the shock Hugoniot data in the several-Mbar range, a fact that is expected given that its primary focus is on near-ambient pressure conditions together with the extreme (P , T) conditions, which are largely devoid of experimental data. In particular, (1) the principal Hugoniot pressure is substantially higher than that measured in experiments (e.g., see Brown *et al.* [57]), and (2) the model’s intersections between the principal Hugoniot and the melt curve (~ 1.9 Mbar and ~ 3.0 Mbar for inception and completion of melting, respectively) are quite off from the currently accepted experimental values, which are 2.25 ± 0.03 Mbar and 2.60 ± 0.03 Mbar, respectively, as reported by Nguyen and Holmes [71]. This in turn means that the Sjöström–Crockett model’s latent heat of melting is very likely to be a few times larger than the actual value in this pressure range.

In this paper, we describe the construction of a five-phase EOS model for Fe. The five phases include the four solid phases mentioned above (α , ϵ , γ , δ) and liquid. Like in our recent paper on developing a multiphase EOS for elemental beryllium (Be) [136], “liquid” in the present study is used as a collective term that represents all fluid phases (e.g., ordinary liquids, gases, supercritical fluids, plasmas) in the wide temperature–density range covered by the EOS. Agreement with DAC and shock data is enforced over the full ranges where these data are available. Given the ongoing debate regarding the two DAC-inferred $T_{\text{melt}}(P)$ curves, we choose to constrain the *baseline* versions of our EOS model to the

TABLE I. Summary of the four multiphase Fe EOS models we present in this paper. We categorize the models into two types: baseline and variation. Here, *baseline* denotes a model that is fit to the full set of experimental thermophysical data deemed in this paper to be robust and suitably constraining, while *variation* denotes a model in which agreement with certain key experimental data is intentionally violated in order to appease agreement with another set of conflicting data. The third column indicates the source of DAC data used for the constraint of $T_{\text{melt}}(P)$, specifically for $P < 3$ Mbar. The fourth column indicates whether or not a particular model satisfies the shock-melting data from Nguyen and Holmes [71]. The fifth column indicates the relationship between the various models' $T_{\text{melt}}(P)$ and different estimations of $T_{\text{melt}}(P)$ constrained by the shock-ramp x-ray diffraction (SRX) experiments from Kraus *et al.* [85], pertaining to $P > 5$ Mbar; see Secs. IV E 1 and V B for details. The two baseline models, min- T_{melt} -SRX and max- T_{melt} -SRX, differ from each other only at pressures above 5 Mbar. As a convenient shorthand, we use the terms “EOS” or “EOS model” to refer to min- T_{melt} -SRX, if not otherwise specified.

Model name	Type	DAC $T_{\text{melt}}(P)$	Shock melt [71]	SRX [85]
		$P < 3$ Mbar	$2.25 \text{ Mbar} \leq P \leq 2.60 \text{ Mbar}$	$P > 5 \text{ Mbar}$
min- T_{melt} -SRX or EOS	baseline	Anzellini <i>et al.</i> [29]	satisfied	lower-bound T_{melt}
max- T_{melt} -SRX	baseline	Anzellini <i>et al.</i> [29]	satisfied	upper-bound T_{melt}
Kraus- T_{melt} -SRX	variation	Anzellini <i>et al.</i> [29]	satisfied	Kraus T_{melt}
low- T_{melt} -DAC	variation	Sinmyo <i>et al.</i> [14] Zhang <i>et al.</i> [11]	not satisfied	lower-bound T_{melt}

$T_{\text{melt}}(P < 3$ Mbar) from the Anzellini *et al.* inference [29], and we have constructed an additional *variation* (denoted low- T_{melt} -DAC) that respects the lower- $T_{\text{melt}}(P < 3$ Mbar) inference of, e.g., Sinmyo *et al.* [14]. We have, in fact, constructed two versions of the baseline models: min- T_{melt} -SRX and max- T_{melt} -SRX. These models differ from each other only at pressures above 5 Mbar, and as their names imply, they span the space of acceptable melt curves when considering recent shock-ramp x-ray diffraction (SRX) data from Kraus *et al.* [85] and their associated uncertainties. In addition, an EOS variation (denoted Kraus- T_{melt} -SRX) that adopts the $T_{\text{melt}}(P > 5$ Mbar) melt curve presented in Kraus *et al.* [85] has also been created and examined along that work's shock-ramp trajectories. None of our EOS models include a thermodynamically stable high-pressure bcc phase since this phase has not been observed in experimental studies [82,85] on *pure* Fe. A summary of the four distinct EOS models generated in this paper—which we divide into two baseline models and two variations—is provided in Table I, and as described further in Appendix C, each of these models is represented in tabular format covering nine orders of magnitude or more in both temperature and density.

It is our hope that the use of these EOS model versions will allow applied scientists (e.g., planetary modelers) to assess uncertainties in their predictions that result from the remaining uncertainties in high-pressure melting. Throughout, we employ modeling strategies that are congruent with our recent paper concerning the construction of a multiphase Be EOS [136], wherein a phase-dependent quasiharmonic ionic-excitation model, and a phase-independent DFT-based atom-in-jellium electronic-excitation model [137,138] are used to represent the thermal portions of the free energy for each phase. Despite its apparent simplicity, we show that good agreement with a host of ambient-pressure, static high-pressure, and dynamic high-pressure experiments can be achieved with this strategy.

The remainder of this paper is as follows: First we introduce the basic functional forms for the free-energy models that we use for each phase (Sec. II), and our new *ab initio* calculations of hcp solid and liquid Fe (Sec. III). Then we

describe the choices we have made to constrain the phase-dependent free-energy models for our baseline EOS models (Sec. IV). The EOS model *variations* (low- T_{melt} -DAC, Kraus- T_{melt} -SRX) and our rationale for creating *two* baseline EOS models (min- T_{melt} -SRX, max- T_{melt} -SRX) are described in detail in Sec. V. Potential applications of the EOS to Earth and planetary science are briefly discussed in Sec. VI. We conclude in Sec. VII.

II. FREE-ENERGY MODELS: FUNCTIONAL FORMS

We assume that the Helmholtz energy $F = E - TS$ (where E is the internal energy and S is the entropy) for each phase of the material admits the decomposition

$$F(\rho, T) = F_{\text{cold}}(\rho) + F_{\text{ion}}(\rho, T) + F_{\text{electron}}(\rho, T), \quad (1)$$

where $F_{\text{cold}}(\rho)$ is the T -independent (so-called, “cold energy” or “cold curve”) piece resulting from expanding or contracting the system (at $T = 0$, when considering solid phases), and $F_{\text{ion}}(\rho, T)$ and $F_{\text{electron}}(\rho, T)$ represent changes to the free energy from ionic and electronic excitations, respectively. Treating ionic and electronic excitations as independent is a manifestation of the Born–Oppenheimer approximation, as is often assumed in EOS studies [133–136,139–142]. We stress, however, that the experimental data to which we fit pertains to the *total* free energy F or the derivatives of F . Any effects from the coupling of electronic and ionic excitations that are manifest in these data are therefore included at some level, provided that our fitting respects these features.

A. Solid phases

To represent the cold term $F_{\text{cold}}(\rho)$ for each crystalline phase, we use both the Vinet analytic form [143] and the Holzapfel AP2 model [144] for the initial fitting. The functional forms adopted by these models and our near-ambient fits to them are presented in Appendix B. Both functional forms are parameterized by the energy minimum E_0 , the density at the minimum energy ρ_0 , the bulk modulus at this density B_0 , and the pressure derivative of the bulk modulus

at this density B' . However, due to the wide range in which we choose to construct our Fe EOS, it is necessary for us to employ forms with significantly more degrees of freedom than just these four numbers. In earlier efforts [140–142], we augmented our Vinet fits with so-called break points [145] for this purpose, but we choose here to employ numerical spline-based cold curves instead, following a similar choice made in our recent Be and Ta EOS work [136,146]. Analytical functions are also employed to smooth these spline-based fits in certain regions, thereby allowing for more smooth pressures and higher-order derivatives of the free energy. Furthermore, additional “knots” (i.e., points where the piecewise polynomials that make up the spline are joined together) are employed only when needed to appease agreement with the combination of static high- P (such as DAC) and shock data, or to improve the connection between the different regimes where disparate sources of data reside. This same combination of spline-based fitting and “hand-tuned” analytical fits are also employed for the ion-thermal Grüneisen parameter $\gamma_{\text{ion}}(\rho)$ described below.

For the ionic-excitation term of the free energy $F_{\text{ion}}(\rho, T)$, we use the Debye model [147],

$$F_{\text{Debye}}(\rho, T) = k_{\text{B}}T \left(\frac{9}{8} \frac{\theta(\rho)}{T} + 3 \ln \left[1 - \exp \left[-\frac{\theta(\rho)}{T} \right] \right] \right) + D \left[\frac{\theta(\rho)}{T} \right], \quad (2)$$

where the Debye integral

$$D(y) = \frac{3}{y^3} \int_0^y \frac{x^3}{\exp(x) - 1}, \quad (3)$$

and $\theta(\rho)$ is the density-dependent characteristic vibrational temperature (i.e., Debye temperature) for the phase in question. This model represents the free energy due to a spectrum of harmonic phonons coupled to a heat bath, wherein the phonon density of states (PDOS) is approximated as a quadratic function of energy up to a cutoff energy $k_{\text{B}}\theta(\rho)$, above which it is taken to be zero. We choose to subsume the first term of Eq. (2), $k_{\text{B}}T \times 9\theta(\rho)/8T = (9/8) k_{\text{B}}\theta(\rho)$, into the $F_{\text{cold}}(\rho)$ of Eq. (1) since it is independent of T (this term arises from the zero-point energy of the phonons). The remainder we take to be the ion-thermal term,

$$F_{\text{ion}}(\rho, T) = F_{\text{Debye}}(\rho, T) - \frac{9}{8} k_{\text{B}}\theta(\rho). \quad (4)$$

Using the Debye model, the high- T Dulong–Petit limit [139–141] ($T > \theta$) of the ionic contribution to the thermal pressure is $P_{\text{ion}}(\rho, T) \rightarrow 3k_{\text{B}}T\gamma_{\text{ion}}(\rho)/V$, where V is the specific volume and $\gamma_{\text{ion}}(\rho)$ is the ion-thermal Grüneisen parameter, equal to

$$\gamma_{\text{ion}}(\rho) = \frac{\rho}{\theta(\rho)} \cdot \frac{d\theta}{d\rho}. \quad (5)$$

In practice, we fit $\gamma_{\text{ion}}(\rho)$ to high- P shock data (which reside in the aforementioned high- T limit), and then determine $\theta(\rho)$ by integrating Eq. (5) along with some knowledge of θ at a reference density as determined by, e.g., ambient-pressure heat-capacity measurements [139]. We find it useful to represent $\gamma_{\text{ion}}(\rho)$ numerically by piecewise linear functions [136], thus furnishing the phase-dependent $\gamma_{\text{ion}}(\rho)$ with more degrees of freedom than that afforded by the simple linear-in- V

fits that we employed in some of our earlier papers [140–142]. We note in passing that while initially designed for the description of the thermodynamics of solids, it has been found that the high- T limit of the Debye model also works well for the low- T EOS of simple monatomic liquids [139–142], and we will therefore employ it in that context too (see Sec. II B).

This assumed form for $F_{\text{ion}}(\rho, T)$ neglects any effects of anharmonicity that might be present at a fixed density ρ [148]. Anharmonicity of this type would lead to deviations of $C_{\text{V}}^{\text{ion}}(T) [\equiv \partial E_{\text{ion}}(\rho, T)/\partial T|_{\rho}]$ from the Debye model value of $3k_{\text{B}}/\text{atom}$ for $T > \theta(\rho)$ [139]. While the neglect of phonon anharmonicity might seem like a gross simplification especially as T approaches T_{melt} , we submit that the sizable effects from $F_{\text{electron}}(\rho, T)$ at these higher temperatures, to be discussed below, should largely outweigh the contributions to the total free energy from anharmonicity for the solid phases of Fe, as we show later in our comparison to the results of DFT-based molecular dynamics (see Figs. 18 and 19).

We take the electronic-excitation contribution to the free energy $F_{\text{electron}}(\rho, T)$ from a DFT spherical-atom-in-jellium model known as PURGATORIO [138], which is an updating of the earlier INFERNO model of Liberman [137]. In this approach, a single representative Fe nucleus is placed at the center of a spherical shell surrounded by a uniform electron-density background. Within the spherical inclusion (the size of which depends upon ρ), the Dirac equation is solved for the states of all 26 electrons using Kohn–Sham DFT at nonzero T , and the results are used to construct the Helmholtz free-energy function, $F_{\text{PURGATORIO}}(\rho, T) = E_{\text{PURGATORIO}}(\rho, T) - T \cdot S_{\text{PURGATORIO}}(\rho, T)$. We then subtract off the $T = 0$ contribution, assigning the remainder to our electron-thermal free-energy term

$$F_{\text{electron}}(\rho, T) = F_{\text{PURGATORIO}}(\rho, T) - F_{\text{PURGATORIO}}(\rho, T = 0). \quad (6)$$

This treatment neglects any directional chemical bonding, given the assumption of spherical symmetry, and it considers only a single representative Fe ion for each (ρ, T) condition (rather than admitting the possibility of multiple distinct charge states, as would necessarily be present in a low- ρ , high- T plasma). However, work has shown that this prescription results in a very sensible electronic free-energy term, if interpreted in the context of Eq. (1), when comparing to the results of multi-ion Kohn–Sham DFT–MD simulations of the EOS of materials at high densities and temperatures [136,142,149,150]. We will discuss this further in Sec. IV, where we compare our EOS models to our DFT–MD simulations of Fe at extreme conditions.

Because PURGATORIO is a spherical-atom-in-jellium construct, it is manifestly agnostic to a notion of crystalline phase. Despite this, we choose to use the PURGATORIO model, as applied in Eq. (6), for the electronic-excitation term for every phase of our free-energy model (including the liquid). While it is the case that the individual phases (α , ϵ , γ , δ , liquid) must each possess distinct $F_{\text{electron}}(\rho, T)$ terms, owing to their different geometric configurations of ions leading to different electronic densities of states, the salient features arising from, e.g., the d -band valence electrons of Fe, are present irrespective of phase at a given (ρ, T) point. Furthermore, the

differences between the true phase-dependent $F_{\text{electron}}(\rho, T)$ functions are likely to be greatest at low T , but this also happens to be where $F_{\text{electron}} \ll F_{\text{ion}}$, generally (i.e., F_{electron} tends to be negligible at low- T conditions where our assumed PURGATORIO model incurs the greatest error) [136,139–142]. This assumption of a single $F_{\text{electron}}(\rho, T)$ model for all phases has been used in our other recent EOS modeling efforts [136] and was also employed (although with a different atom-in-jellium model) in the Sjoström–Crockett Fe EOS [135]; its efficacy rests on the fact that the primary differences between the thermodynamic properties of various phases of a typical metal are due to differences in their cold and vibrational contributions.

The strategy of Eq. (6) exhibits a subtlety that we now address. The cold curve of the PURGATORIO model for any element (and for Fe in particular), which we denote as $F_{\text{PURGATORIO}}(\rho, T = 0)$, possesses a minimum at some ρ that is different from the ρ_0 values of the cold curves of each of the individual phases. This minimum is spurious, given that it pertains strictly to the fictitious spherical average-atom “solid”. But even after the subtraction mandated by Eq. (6), the resulting $F_{\text{electron}}(\rho, T)$ exhibits the remnants of these unphysical features at low ρ . We rid our $F_{\text{electron}}(\rho, T)$ model of these artifacts by employing the strategy outlined in the discussion surrounding Eq. (10) in our Be EOS publication [136], where the PURGATORIO electron-thermal free energy is effectively replaced by extrapolations based on the density scaling of the associated Thomas–Fermi [151,152] contribution for $\rho < \rho_b = 5.4 \text{ g/cm}^3$ (for the Be EOS construction, a different value for ρ_b was used, and a temperature T_b above which no correction was applied was also defined). This prescription leads to a $F_{\text{electron}}(\rho, T)$ that is reasonably well behaved throughout the full range of our interest.

For the α phase, we augment $F_{\text{electron}}(\rho, T)$ with an additional term, which accounts for the effects of magnetic ordering, given that this phase is known to possess large, preferentially oriented magnetic moments coming from its valence electrons. We take the empirical ρ -independent magnetic-excitation term used in both the Boettger–Wallace [130] Fe EOS and the Sjoström–Crockett [135] Fe EOS for this term {called F_{mag} ; see Eq. (7) in Boettger and Wallace [130] and Fig. 5 in Sjoström and Crockett [135]}. Its inclusion allows us to obtain the correct divergence in the specific heat of α -phase Fe at the Curie temperature, $T = 1043 \text{ K}$, and low P [153]. Although it is generally small compared to the other terms we have discussed (and contributes nothing to the pressure because of its ρ -independent nature), we have found that including it does have some effect on our fitting of the $F_{\text{ion}}(\rho, T)$ term for the α phase, when constraining to low- P experimental data.

B. Liquid phase

Liquids, unlike solids, cannot be viewed as occupying a localized region of phase space (ionic positions and momenta: $\{\mathbf{r}_{\text{ion}}, \mathbf{p}_{\text{ion}}\}$) centered around some perfect arrangement of stationary ions. Yet it has been shown repeatedly that the thermophysical properties of dense one-component liquids for T just above $T_{\text{melt}}(P)$ are much like that of high- T crystalline solids [136,139,140,142,154,155]. In particular, once

a reasonable estimation of F_{electron} is assumed, the remaining $F(\rho, T) - F_{\text{electron}}(\rho, T)$ can be fit well by the sum of suitably chosen $F_{\text{cold}}(\rho)$ and $F_{\text{ion}}(\rho, T)$ terms, the latter of which is well described by a Debye model [140,142,154,155] with an effective Debye temperature, which is lower than that of the solid (thereby endowing the liquid with a higher entropy than the solid at a given set of ρ and T conditions). This is possible largely because the ionic component to the isochoric specific heat is very nearly $3k_B$ /atom for monatomic systems for T up to at least $2T_{\text{melt}}(P)$ (see [136,140,142,156], as well as our *ab initio* DFT–MD results for Fe presented in Sec. III and Appendix A). The behavior of the liquid EOS ultimately transitions to $C_V^{\text{ion}} \rightarrow \frac{3}{2}k_B$ /atom (the ideal-gas limit) at sufficiently high T [135,136,142]. Other properties similarly approach the ideal-gas limit as well.

A number of additions to the Debye model exist (such as the Cowan model, as applied in Refs. [140–142]), which help to enforce this limiting behavior; we use our so-called Cell model [136,142,157], which treats the ions in a high- T [$\gg \theta(\rho)$] liquid as distinguishable particles, each of which moves in a fixed, density-dependent potential (centered at zero ionic displacement) consisting of an r^2 term joined to a spherical hard-wall boundary of radius R . The resulting ion-thermal free energy is

$$F_{\text{ion}}(\rho, T) = F_{\text{Debye}}(\rho, T) - \frac{9}{8}k_B\theta(\rho) - k_B T \ln \left[\text{erf} \left(\sqrt{\frac{T^*}{T}} \right) - \frac{2}{\sqrt{\pi}} \sqrt{\frac{T^*}{T}} \exp \left(-\frac{T^*}{T} \right) \right], \quad (7)$$

where $k_B T^*$ is the ρ -dependent energy at which the r^2 and hard-wall portions meet,

$$k_B T^*(\rho) = \frac{m_{\text{ion}} k_B^2 [\theta(\rho) R(\rho)]^2}{2\hbar^2}, \quad (8)$$

and

$$R(\rho) = \left[\frac{3m_{\text{ion}} e}{4\pi\rho} \right]^{1/3}. \quad (9)$$

This form for the ion-thermal free energy has the property that $\lim_{T \rightarrow \infty} E_{\text{ion}}(\rho, T) = 3k_B T/2$ per ion, and $\lim_{T \rightarrow \infty} P_{\text{ion}}(\rho, T) = k_B T \rho / m_{\text{ion}}$, as desired. The $e = \exp(1)$ in Eq. (9) ensures that the proper ideal-gas entropy for the ions is achieved as $T \rightarrow \infty$. We have found the Cell model to be a satisfactory approach when constraining an EOS to high- T computational predictions of E and P coming from, e.g., path-integral Monte Carlo simulations [142] or specialized DFT-based methods targeted for high temperatures, such as SQDFT [158].

We therefore adopt the same three-term decomposition presented in Eq. (1) for our liquid Fe free-energy model, where the F_{ion} term is taken to be that in Eqs. (7)–(9) and our F_{electron} contribution is taken from the PURGATORIO model. Two additional points must now be addressed, both of which pertain to the fact that the liquid occupies the full density range over which our EOS is defined. First, for very high ρ ($> 100 \text{ g/cm}^3$), we choose to require that $F_{\text{cold}}^{\text{liquid}}(\rho)$ joins on to the PURGATORIO $F_{\text{cold}}(\rho)$ for Fe. This is because we know the PURGATORIO cold curve to be an accurate

representation of the high- ρ Kohn–Sham DFT cold curve (assuming the use of identical exchange–correlation functionals) as computed with the usual multi-ion DFT framework (irrespective of crystalline phase) for all elemental materials. We mandate this high- ρ connection with spline interpolation, joining to our lower- ρ $F_{\text{cold}}^{\text{liquid}}(\rho)$ as determined by fitting to various experimental data (see Sec. IV E). Likewise, we require that $\gamma_{\text{ion}}^{\text{liquid}}(\rho)$ tends to $1/2$ as $\rho \rightarrow \infty$, as required by basic considerations of its limiting behavior [159]. The second point we make is that for low ρ , our liquid free-energy model must possess the requisite structure to admit a liquid–vapor transition, which is crucial to include if our Fe EOS is to be applied to the study of planetary–collision and impact phenomena [41]. We enforce a liquid–vapor transition region by joining the low- ρ portion of $F_{\text{cold}}^{\text{liquid}}(\rho)$ to something akin to a soft-sphere model [145] (although in practice, we use a pointwise numerical form with a similar shape), which possesses a concave-down portion for $\rho < \rho_0$ smoothly joined to a ρ -independent piece in the dilute limit $\{\rho \ll \rho_0$; where $\lim_{\rho \rightarrow 0}[F_{\text{cold}}^{\text{liquid}}(\rho) - E_0] = \text{the cohesive energy}\}$. The liquid–vapor dome can then be obtained by applying the Maxwell construction [139] within the resulting $F_{\text{liquid}}(\rho, T)$, restoring convexity to this function [133,134,145,160].

After fixing the electron-thermal term for each phase to be that of the PURGATORIO model in Eq. (6) {and after setting the additional $F_{\text{mag}}(T)$ term for the α phase to be that from [130]}, we are left with two ρ -dependent functions that must be specified for each of the five phases of our Fe EOS: $F_{\text{cold}}^i(\rho)$, and $\theta^i(\rho)$ [see Eqs. (1), (2), (4), (8)], where i denotes the phase. It is helpful to think of $F_{\text{cold}}^i(\rho) - F_{\text{cold}}^j(\rho)$ as controlling the internal energy difference between phases i and j , and $3k_B \ln[\theta^i(\rho)/\theta^j(\rho)]$ as being the major contributor to the entropy difference (at least for $T > \theta^i, \theta^j$) [140]. In Sec. IV, we describe how our choices for these 10 functions (F_{cold} and θ for all five phases) arise from fitting to a host of static- and dynamic-compression data taken on Fe.

III. AB INITIO CALCULATIONS

We have performed DFT–MD for Fe over a restricted range of compressions and temperatures that are relevant to geophysical applications like those mentioned in the Introduction. We discuss below (in Secs. IV B and IV E) that for two of the five phases of our model, namely the ϵ and liquid phases (especially the latter), we consult these predictions when faced with a paucity of constraining experimental information. It should be kept in mind that any particular variant of DFT involves approximations, specifically in regard to the choice of exchange–correlation functional. Thus, perfect agreement between such predictions and experiment, where such data coincide in (ρ, T) , is not expected, although the calculations tend to give reasonable results if care is taken with respect to the various approximations involved. However, qualitative agreement for EOS-related quantities necessarily buttresses our confidence in the data and hence in any EOS model that uses them as constraints.

Our Fe DFT–MD simulations provide calculations of the internal energy $E(\rho, T)$ and pressure $P(\rho, T)$ on a dense grid of densities ρ and temperature T . These were performed

with the VASP code [161–164] using the PBE exchange–correlation functional [165,166], with its 16-valence-electron PAW pseudopotentials [167,168], a plane-wave energy cut-off of 500 eV, and a single k point at $(1/4, 1/4, 1/4)$. The electronic temperature was set equal to the average ionic temperature, and a Nosé–Hoover thermostat [169,170] was employed. The MD timestep was set to 1 fs. For each DFT–MD simulation, 256 atoms were placed in a box with periodic boundary conditions, and E and P were averaged over 10^4 snapshots (over a time interval of 10 ps) to produce the $E(\rho, T)$ and $P(\rho, T)$ predictions. The (ρ, T) grid includes seven isochores between $\rho = 12.0$ and 18.0 g/cm³, and temperatures in increments of 1000 K, from 4000 to 12000 K. The larger- ρ , lower- T simulations were performed in the hcp phase of Fe, while the lower- ρ , higher- T points were initialized as liquid. For a narrow band of these grid points (roughly 4000 K wide in T), both solid and liquid calculations of E and P were performed; this band was chosen to surround the region where we expected the equilibrium melt curve to intersect the principal Hugoniot, given previous studies [29,125]. We include our DFT–MD P and E predictions for hcp and liquid phases of pure Fe in Appendix A, along with a brief discussion of comparisons between these E and P predictions and those of our EOS.

IV. BASELINE EOS MODELS: PHASE-DEPENDENT FITTING

In this section, we outline our multipronged strategy for constraining the phase-dependent EOS model inputs [$F_{\text{cold}}^i(\rho)$ and $\theta^i(\rho)$; $i = \text{phase}$]. The constraints we use are summarized in Table II. Our detailed methodology is described, for each individual phase, in the subsections that follow (Secs. IV A–IV B). In the liquid phase subsection (Sec. IV E), we include detailed discussions of our determination of both compression and expansion regimes of the free energy, as well as our strategy for using recent experimental inferences of high-pressure melting to further constrain the model. This section concerns primarily the fitting of our baseline EOS models, which are labeled as min- T_{melt} -SRX and max- T_{melt} -SRX in Table I. Section V discusses the two other versions of our EOS listed in that table. Namely, Sec. V A includes a detailed description of our low- T_{melt} variation to our Fe EOS motivated by conflicting DAC studies (addressing $P < 3$ Mbar); in Sec. V B, we describe our motivation for creating the two baseline models (as well as the Kraus- T_{melt} -SRX variation) that stem from uncertainties in the precise trajectory of $T_{\text{melt}}(P)$ for $P > 6$ Mbar.

A. α (bcc; lower- T)

Because the α phase of Fe is the ambient phase [see the Fe phase diagram plots Figs. 1(a) and 1(b) to which we shall return throughout the entirety of Sec. IV], there is a relatively large amount of highly constraining thermophysical data that can be used to fit our α -phase free-energy model. These data, taken over many years and by different researchers, are largely consistent with each other. Thus, we fix our gaze on a restricted set of α -phase measurements, including both ambient-pressure (1-bar heat capacity and thermal expansion)

TABLE II. Summary of the phase-dependent experimental and theoretical (in the case of DFT–MD) information used to constrain the free-energy models of our Fe EOS. Here, “DAC” indicates measurements conducted in a diamond-anvil cell, and “RT” stands for room temperature. The DFT–MD (this paper) entries listed in the last column refer to those calculations performed in the present paper, which are the focus of Sec. III. Some representative references are listed here, but we refer the reader to the text for a complete enumeration of all the sources we have used to constrain/test our EOS. The (T, P) conditions listed for the Hugoniot curves refer to the initial conditions where the shock compression was initiated.

Phase	Isobar	DAC	Hugoniot [171]	Phase boundary	Calculation
α (bcc)	1 bar $S(T)$ [4], 1 bar $\rho(T)$ [172]	RT isotherm [25]	300 K, 1 bar [63] Shock release [68]	α – γ , α – ϵ	
γ (fcc)	1 bar $S(T)$ [4], 1 bar $\rho(T)$ [172]		1573 K, 1 bar [69] Shock release [68]	γ –liquid, γ – ϵ	
δ (bcc)	1 bar $S(T)$ [4], 1 bar $\rho(T)$ [172]			δ –liquid, δ – γ	
ϵ (hcp)		RT isotherm [25,28]	300 K, 1 bar	ϵ –liquid, ϵ – γ Shock melting [41,71,85]	DFT–MD (this paper)
liquid	1 bar $S(T)$ [4] 1 bar $\rho(T)$ [1–3]		300 K, 1 bar	DAC melt [29] Shock melting [41,71,85]	DFT–MD (this paper)

and higher-pressure (room- T static-compression isotherm and principal shock Hugoniot) experimental data.

As explained in Sec. II and shown in Eq. (1), construction of the EOS requires us to determine two different terms, representing the cold F_{cold} and ion-thermal F_{ion} contributions, to the total free energy of each phase. (The third term F_{electron} , which represents the electron-thermal contribution to the free energy, is fixed by assumption to be that of the PURGATORIO model.) For the ion-thermal contribution of the α phase, we use 1-bar T -dependent thermal-expansion [172] [i.e., $\rho(T)$] and entropy [4] data, the latter of which are derived from specific-heat measurements. This allows us to constrain both the ion-thermal Grüneisen parameter γ_{ion}

and the Debye temperature θ of α -Fe in the neighborhood of the ambient density, 7.874 g/cm^3 . Figure 2(a) displays our fit to the 1-bar thermal-expansion data, including not just the α phase (below $\sim 1250 \text{ K}$), but γ , δ , and the liquid as well (to be discussed below). Likewise, Fig. 2(b) shows our fit to the 1-bar entropy data, the lowest 10 points of which pertain to α -Fe. In addition, the ion-thermal term has a strong influence on the principal Hugoniot, and Fig. 3(a) shows such data for α -Fe, which cover a slightly higher-density range than the 1-bar thermal-expansion data. Our major constraint for the cold term comes from the 300 K DAC pressure isotherm of Dewaele *et al.* [25], which covers a range that includes both the α and ϵ phases. Our fit

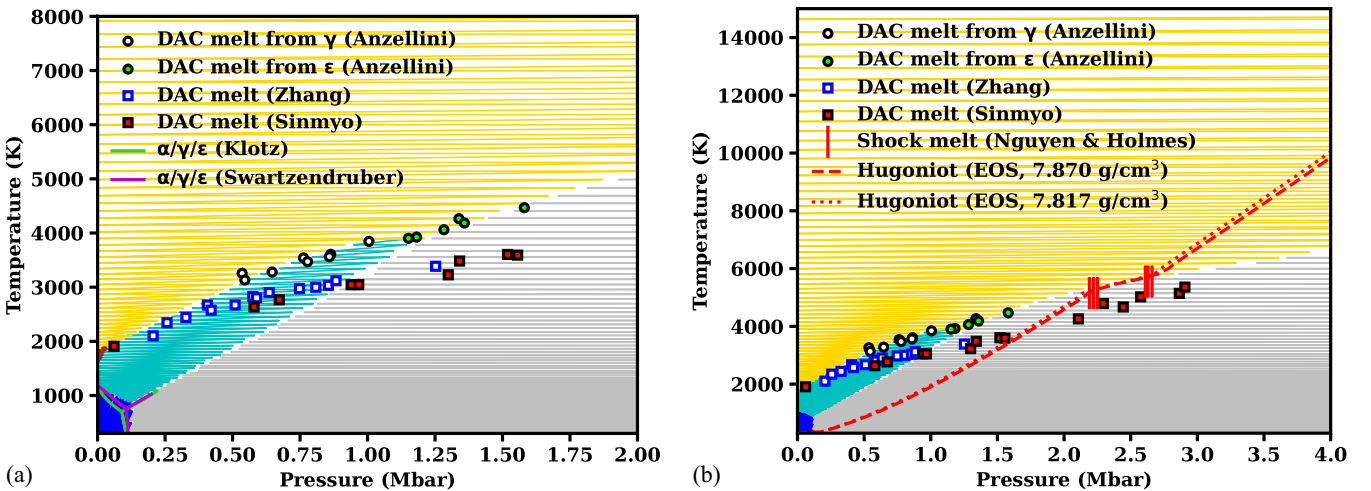


FIG. 1. Fe phase diagram from our multiphase EOS for two pressure ranges: (a) $P \leq 2 \text{ Mbar}$ and (b) $P \leq 4 \text{ Mbar}$, respectively. Blue indicates the α phase (ambient bcc), gray indicates ϵ (hcp), cyan indicates γ (fcc), brown (just below T_{melt} near $P = 0$) indicates δ (high-temperature bcc), and orange indicates the liquid. Principal Hugoniot curves for our EOS at two different starting densities (corresponding to those reported in Nguyen and Holmes [71]) are indicated by the red dashed and dotted lines in the (b) panel. Also displayed are various points from experimental determinations of the melt curve, and shock-melt pressures from Nguyen and Holmes (vertical red bars, where we have also included error bars on their reported uncertainties in pressure). The magenta solid curves that appear below 0.25 Mbar in (a) indicate experimentally reported $\alpha \rightarrow \epsilon$, $\alpha \rightarrow \gamma$, and $\gamma \rightarrow \epsilon$ phase-transition curves [173,174]. Due to space limitations, in this figure and in all subsequent figures, we include the name of only the first author in the label for each reference that involves three or more authors.

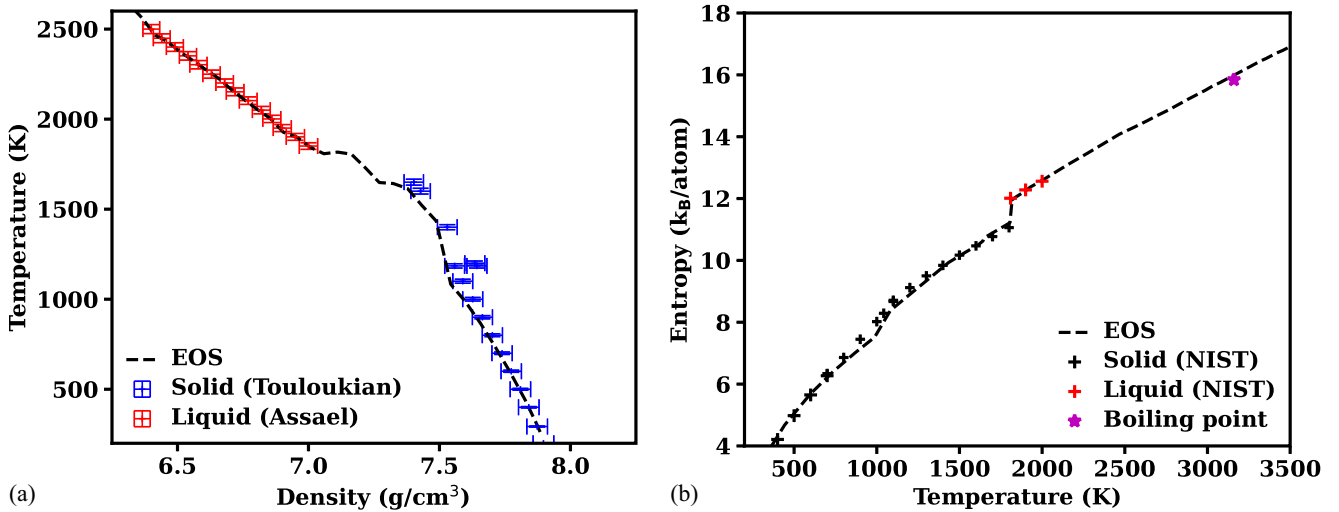


FIG. 2. (a) Ambient-pressure thermal-expansion data from (solid [172]; blue symbols) and (liquid [1–3]; red symbols), and the 1-bar $\rho(T)$ isobar from our EOS (dashed line); and (b) ambient-pressure entropy from experiments [4] (symbols) and our EOS (dashed line).

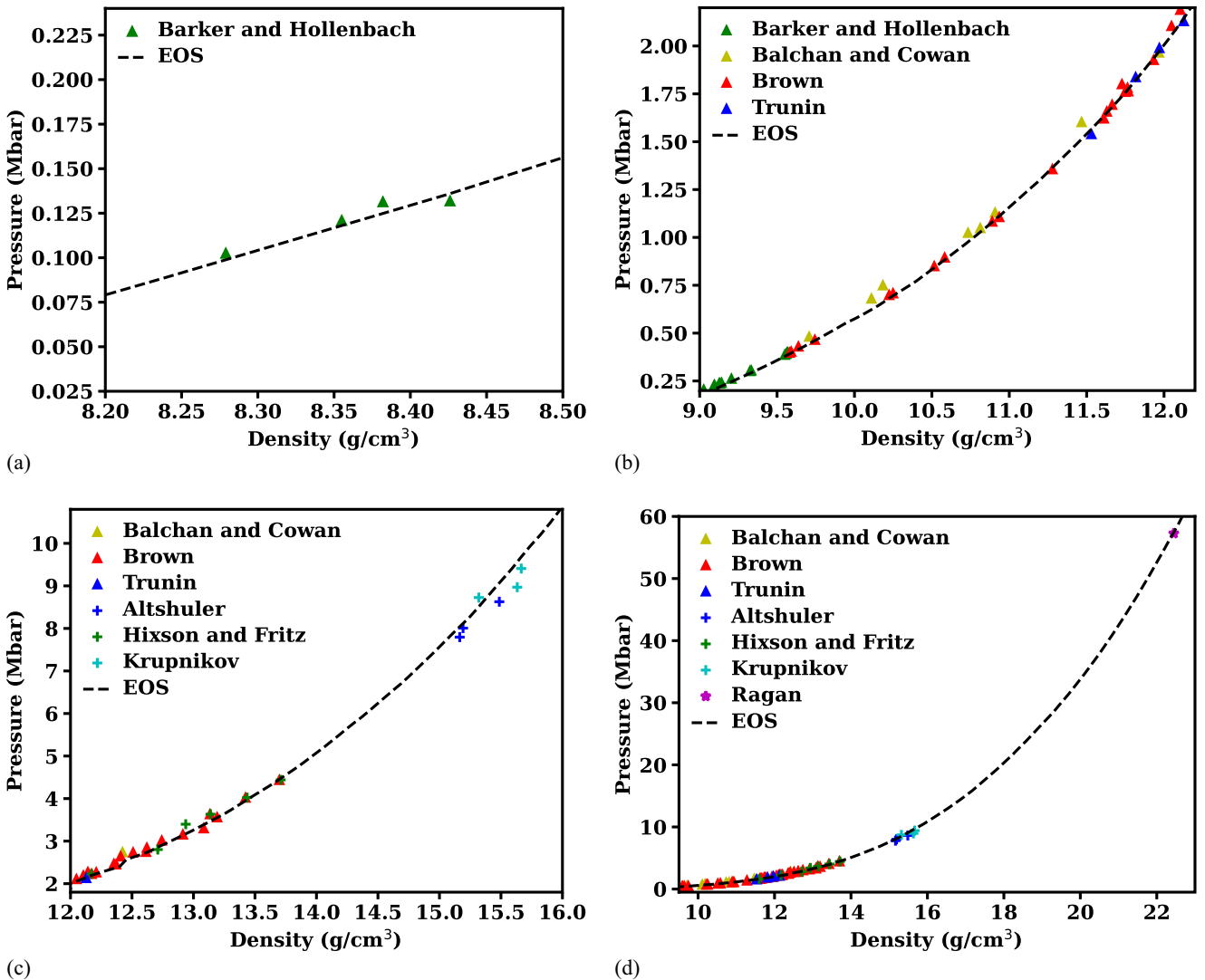


FIG. 3. Principal Hugoniot of Fe covering different pressure ranges and different thermodynamic stability fields: (a) $P \leq 0.15$ Mbar (α phase [bcc]), (b) $0.2 \text{ Mbar} \leq P \leq 2.2$ Mbar (ϵ phase [hcp]), (c) $2 \text{ Mbar} \leq P \leq 10$ Mbar (liquid), and (d) $P \leq 60$ Mbar (high- P liquid), respectively. Symbols correspond to experimental measurements, and the dashed lines are from our EOS model.

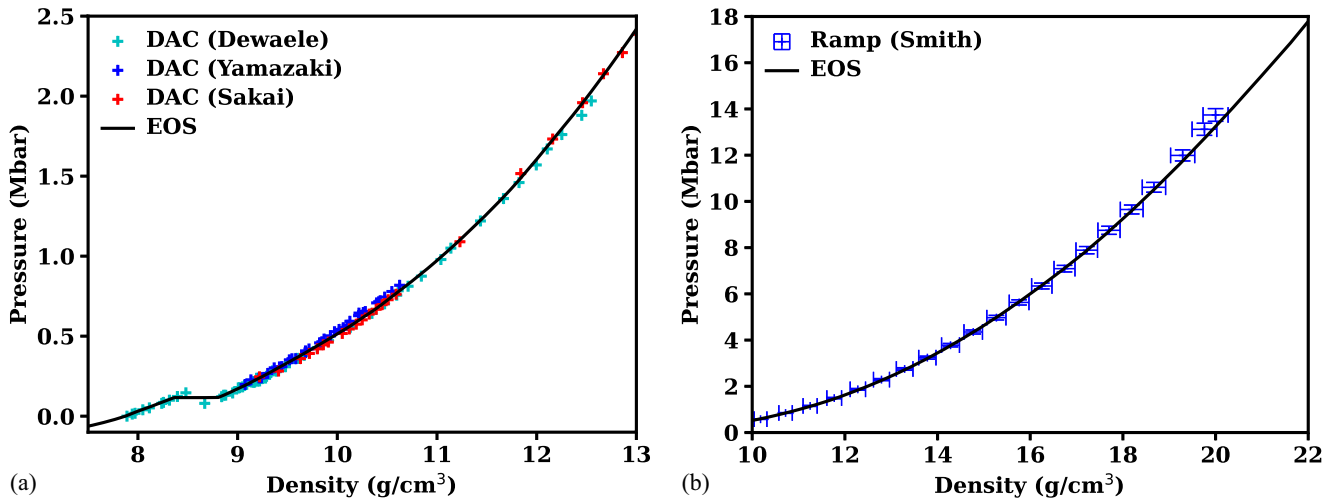


FIG. 4. (a) Room-temperature isotherm data from the DAC measurements of selected references [25,28,31] (symbols), and the corresponding isotherm from our EOS in the regime of stability for α (bcc) and ϵ (hcp) phases (black line). (b) NIF ramp-compression data from Smith *et al.* [42] (symbols), and the principal isentrope from the EOS (black line).

to the 300-K pressure-isotherm data of Dewaele *et al.* [25], Yamazaki *et al.* [28], and Sakai *et al.* [31] is shown in Fig. 4(a), where the portion for $P < 0.13$ Mbar corresponds to the α phase.

B. ϵ (hcp)

Since the ϵ phase is not stable at ambient pressure (see Fig. 1), we lack the T -dependent thermal-expansion and absolute-entropy data that we have for α , γ , δ , and the liquid. Instead, our main experimental constraints pertain to the stability of this phase relative to that of α and γ , pressure-isotherm data from DAC [25], shock data along the principal Hugoniot curve (i.e., with initial conditions of $\rho_0 \sim 7.874$ g/cm³ and $T_0 = 300$ K) from multiple studies [43–58], and recent ramp-compression data from Lawrence Livermore National Laboratory’s National Ignition Facility (NIF) [42]. Above 2.25 Mbar, the experimental work of Nguyen and Holmes [71] shows the Hugoniot final states to be either in a solid–liquid mixed phase state or in the pure liquid. Thankfully, the literature includes many Hugoniot points with pressures between 0.13 and 2.25 Mbar, and hence within the pure ϵ -phase region. These data, along with the 300-K pressure isotherms of Dewaele *et al.* [25] and Sakai *et al.* [31], provide us with enough constraints to determine both $F_{\text{cold}}(\rho)$ and $\gamma_{\text{ion}}(\rho)$ for ϵ up to $\rho \sim 12.75$ g/cm³, the highest ρ point shown in Fig. 4(a). From roughly 9–12 g/cm³, we also have principal Hugoniot data that are still in the ϵ phase [as shown in Fig. 3(b)], but we lack highly constraining and consistent fixed- T isotherm data. For densities above 12.75 g/cm³, we have neither constraining DAC data nor Hugoniot data for ϵ -phase final states [71]. However, the NIF ramp-compression data [42], which are *ostensibly* in the ϵ phase, are available for pressures up to 14 Mbar (and densities up to ~ 20 g/cm³). We constrain to these data by assuming that they lie on the principal isentrope of Fe; since this isentrope should be very close to the 300-K isotherm in ρ - P space, it serves mainly as a constraint for the $F_{\text{cold}}(\rho)$ of ϵ .

Figure 4(b) shows the NIF ramp-compression data up to $P = 14$ Mbar, along with the isentrope of our ϵ -phase free-energy model after suitable constraints have been applied. Above this pressure, we have no (quasi-)isentropic data for Fe at the time of this writing. We must therefore appeal to the predictions of *ab initio* electronic-structure calculations for EOS information at larger compressions, which we do by referring to the ϵ -phase cold curve as computed [175] by an all-electron DFT method using the Perdew–Burke–Ernzerhof (PBE) exchange–correlation functional [165,166]. For $\rho > 100$ g/cm³ we morph the ϵ -phase $F_{\text{cold}}(\rho)$ into that of PURGATORIO, as we do for the liquid, described above in Sec. II B.

Figure 5(a) shows the cold energies of the α and ϵ phases from our EOS (along with those of the other phases; see the discussions below), near ambient density. Note that the large $\Delta\rho$ between the minima of $F_{\text{cold}}^{\alpha}(\rho)$ (solid blue curve) and $F_{\text{cold}}^{\epsilon}(\rho)$ (dashed-dotted black curve) reflects the sizable volume change seen in the $\alpha \rightarrow \epsilon$ transition that is discussed in the study by Boettger and Wallace [130] and references therein. Additionally, we see that the resulting minima of $F_{\text{cold}}^{\text{liquid}}(\rho)$, $F_{\text{cold}}^{\gamma}(\rho)$, and $F_{\text{cold}}^{\delta}(\rho)$ are each far closer to that of α than to that of ϵ , as required by the thermal-expansion data [1–3,172] in Fig. 2(a).

The discussion thus far pertains primarily to our constraint of $F_{\text{cold}}(\rho)$ for all ρ , together with our constraint of $\gamma_{\text{ion}}(\rho)$ for $\rho < 12.5$ g/cm³, both for the ϵ phase. We must still choose the ionic Grüneisen parameter at higher densities, followed by $\theta(\rho)$ at *some* value of ρ [from which the full ρ -dependent curve will then follow, according to Eq. (5)]. For the latter, we appeal to the fact that the $\alpha \rightarrow \epsilon$ phase transition occurs at $P \sim 0.13$ Mbar (Fig. 4), and this transition pressure decreases slowly as T is increased [130]. Figure 5(b) shows the $\theta(\rho)$ for each phase after this fitting (and the fitting described in subsequent sections, for other phases) has been performed. Note that $\theta^{\alpha}(\rho)$ is relatively close to $\theta^{\epsilon}(\rho)$, a consequence of the relative independence of the $\alpha \rightarrow \epsilon$ transition pressure on T . The precise relationship, showing crossings at around

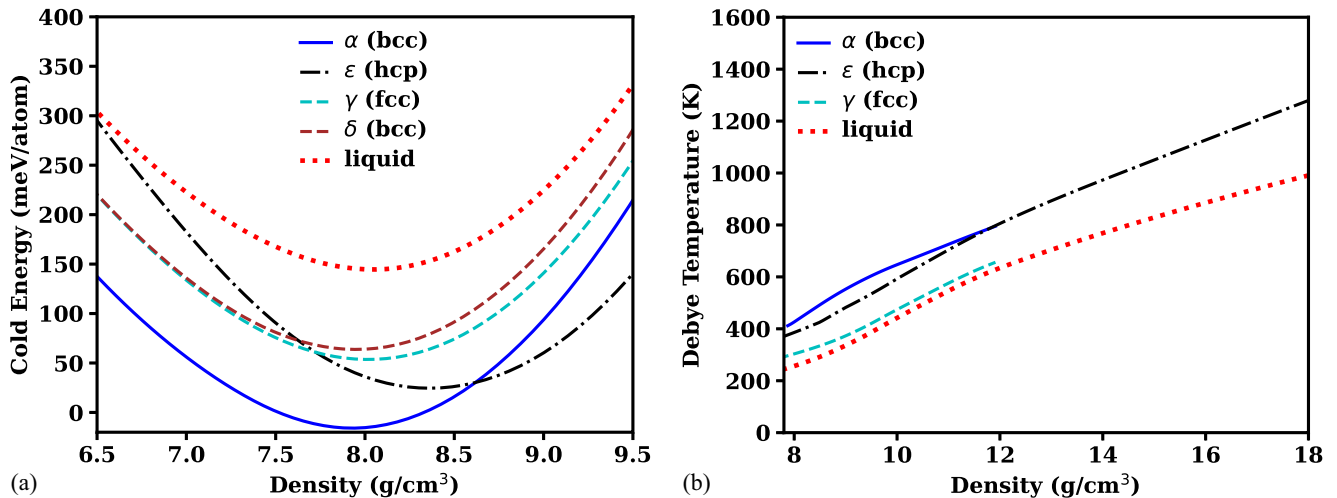


FIG. 5. (a) Phase-dependent cold energy curves, $F_{\text{cold}}(\rho)$, for our multiphase Fe EOS in the neighborhood of ambient density. (b) Density-dependent Debye temperatures $\theta(\rho)$ for four out of the five phases (excluding the δ phase) over a slightly wider range of density than shown in (a). The liquid $\theta(\rho)$ is the lowest, owing to that phase's largest entropy, followed by $\theta^\gamma(\rho)$.

12 g/cm³, is needed to reproduce the experimentally determined α – ϵ phase line in detail, given the specific $F_{\text{cold}}^\alpha(\rho)$ and $F_{\text{cold}}^\epsilon(\rho)$ we have employed. Additional comparisons to our DFT–MD predictions of $P(\rho, T)$ in the ϵ phase (see Appendix A) informs our choice of $\gamma_{\text{ion}}(\rho)$ for $\rho > 12.5$ g/cm³, completing our specification of the free-energy model of this phase, though small tweaks to our $F_{\text{cold}}^\epsilon(\rho)$ and $\theta^\epsilon(\rho)$ functions were made subsequent to the application of the above constraints, to appease agreement with the ϵ – γ phase line.

C. γ (fcc)

The γ phase of Fe is observed to be thermodynamically stable below about 1 Mbar [Figs. 1(a) and 1(b)], and Fe is believed to melt out of this phase in this pressure range. Like in the case of the α phase, we use the 1-bar $S(T)$ and $\rho(T)$ data of Refs. [4,172] as constraints for the lowest- ρ portions of $F_{\text{cold}}(\rho)$ and $\theta(\rho)$ [Figs. 2(a) and 2(b)]. Additional constraints on the ρ dependence of these functions are supplied by experimental data on the α – γ and ϵ – γ phase lines [18]. The principal Hugoniot (i.e., the Hugoniot starting in the normal ambient conditions, in the α phase) has no final states within the stability field of the γ phase, meaning that it misses that phase entirely. The only way to shock into γ is therefore to shock from a preheated initial state, and this was accomplished by Chen and Ahrens in 1997 in their attempt to characterize the γ -phase EOS for planetary-science applications [69]. Their Hugoniot points, starting from a ($P = 0$, $T = 1573$ K) initial state, are shown in Fig. 6(a), along with the same Hugoniot as rendered by our γ -phase free-energy model, after (admittedly imperfect) agreement with these data is achieved by bending the higher- ρ portions of our $F_{\text{cold}}(\rho)$ and $\gamma_{\text{ion}}(\rho)$ functions appropriately.

For experimental confirmation on the lower- P portion of our γ -phase free-energy model, we turn to the shock–release measurements of Zhernokletov *et al.* [68], in which releases to various lower-stress states were observed after shocking to ~ 1.5 Mbar. Figure 6(b) shows these points in the plane of

pressure versus particle velocity (u_p ; blue symbols). Assuming the release to be isentropic, we compare to the isentrope (dashed curve) of our EOS that intersects the 1.5 Mbar shock state, as determined by the Hugoniot of our model (solid curve). We note that we did not use the points of Fig. 6(b) as constraints in our fitting, yet the agreement is excellent. Since the lowest three ($P < 0.5$ Mbar) of these measured release points reside within the γ phase, this provides a strong confirmation of the accuracy of the low- P portion of our γ free-energy model.

D. δ (high- T bcc)

The δ phase occupies an exceedingly small range of pressure and temperature in the Fe phase diagram [see Ref. [18], also shown in Fig. 1(a)]; this phase covers an approximate T – P range of $P < 0.05$ Mbar, and T between 1650 and 1811 K. As such, it is unnecessary (and impossible, from experimental data) to construct $F_{\text{cold}}(\rho)$ and $\theta(\rho)$ functions pertaining to it which cover a substantial range of ρ . The comprehensive thermal-expansion data of Abdullaev *et al.* [3] provides us with the means to determine the product of γ_{ion} and the bulk modulus (given the specific heat), and the entropy data in the NIST heat-capacity database [4] [see Fig. 2(b)] provides a suitable constraint on θ . The position of δ relative to γ and liquid in the phase diagram then yields a unique determination of the difference between the cold curve of δ and that of the other phases at the relevant densities.

E. Liquid

The liquid is the only phase that is stable over the full range of compression (since as we mentioned in Sec. I, what we refer to as the liquid includes all fluid phases encompassed by our EOS), and we must represent its free energy at temperatures in the range from $T \in [T_{\text{melt}}(\rho), \infty)$ at each ρ . The mandate that the liquid EOS reaches the ideal-gas EOS at sufficiently high T is satisfied by our

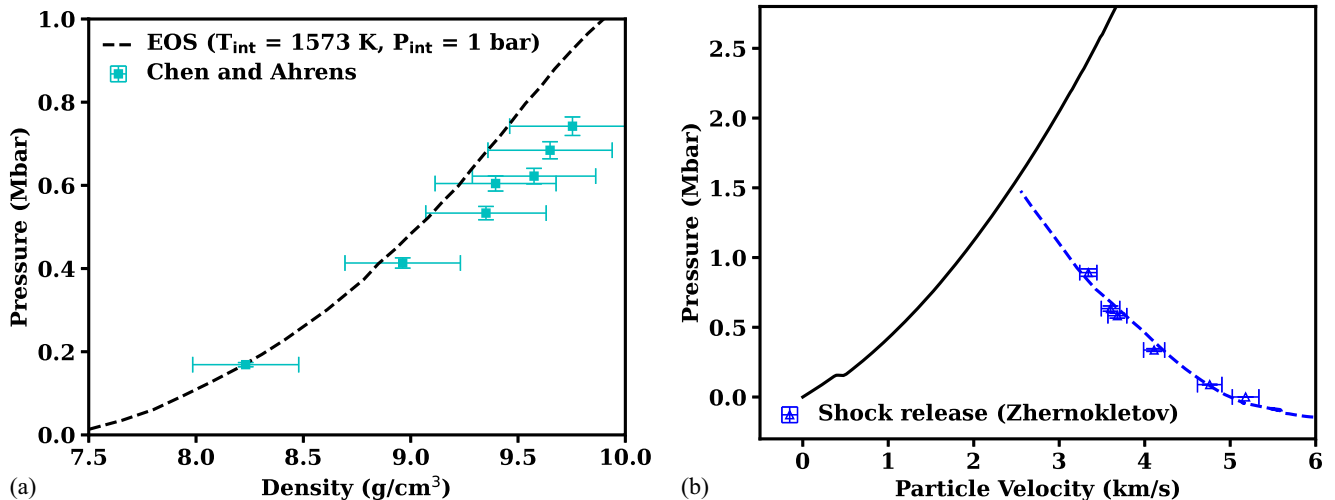


FIG. 6. (a) Hugoniot for a liquid initial state at ambient pressure and $T_0 = 1573$ K. Symbols correspond to experimental measurements [69], and the dashed curve is from the EOS. The final states represented by these data are believed to reside within the γ phase. (b) Shock-release data in the P - u_p plane (blue symbols) [68] along with our EOS model's principal Hugoniot (solid curve) and assumed isentropic release (dashed curve) from a given shock state at about 1.5 Mbar. The lowest- P release states ($P < 0.5$ Mbar) should reside within the γ field of stability.

$F_{\text{ion}}^{\text{liquid}}(\rho, T)$ and $F_{\text{electron}}(\rho, T)$ models of Eqs. (6)–(9); however, we must additionally determine suitable $F_{\text{cold}}^{\text{liquid}}(\rho)$ and $\theta^{\text{liquid}}(\rho)$ functions to attain agreement with a host of liquid phase ambient-pressure thermal-expansion and entropy data, as well as high-pressure shock data. Unlike for the α and ϵ phases, we lack isothermal constraints from DAC; in their stead, we have the important constraint of a *prescribed melt curve* $T_{\text{melt}}(P)$, and it is here that we are forced to choose *which* of the recent experimentally determined melt curves to assume. Below $P = 3$ Mbar, there are two distinctly different $T_{\text{melt}}(P)$ curves motivated by DAC studies, which we label “higher- T_{melt} ” (see, e.g., Ref. [29]) and “lower- T_{melt} ” (see, e.g., Refs. [14,26]). We choose the higher- T_{melt} values as the constraint to our EOS model, largely because we deem them to be in better agreement with shock-melt data [71]. However, we will present in Sec. V A our *variation* to the present Fe EOS (which we name low- T_{melt} -DAC, as indicated in Table I), appealing agreement with the lower- T_{melt} inferences [14,26] while sacrificing shock-melt agreement. Likewise, there is still uncertainty in $T_{\text{melt}}(P)$ for $P > 3$ Mbar, despite the fact that recent shock-ramp *in situ* x-ray diffraction experiments have provided important new constraints in the $5 \text{ Mbar} < P < 10 \text{ Mbar}$ range. We discuss our use of these data in Secs. IV E 1 and V B, in the context of the two baseline EOS models and our Kraus- T_{melt} -SRX EOS model variation.

We divide our discussion on the baseline liquid model into the following two subsections, depending on whether we are interested in densities indicative of compression or expansion. The focus of the latter subsection on the expansion region is the liquid-vapor dome, which is important for applications like Earth-core vaporization due to giant impacts [41].

1. Compression region

First, we address the single-phase liquid Fe EOS data at near-ambient densities, including measurements of $\rho(T)$ and

$S(T)$ at ambient pressure. We fit the $\rho(T)$ data [1–3] in the usual way, by constraining the near-ambient- ρ portions of both $F_{\text{cold}}(\rho)$ and $\gamma_{\text{ion}}(\rho)$ (though the absolute scale of F_{cold} must be set in relation to the other phases’ cold energies, through our matching to T_{melt} ; see below). The result of this fitting has been shown in Fig. 2(a). For the $S(T)$ entropy constraint, the NIST data [4] contains several experimentally inferred points just above $T_{\text{melt}}(P = 1 \text{ bar})$ [see the red points in Fig. 2(b)], and then another at the boiling point roughly 1000 K higher in temperature. In these NIST tables, more points than just these four in the liquid regime are presented, but it is our understanding that the intervening values are derived from an assumed low-pressure liquid EOS model. Thus, we restrict our fitting to just these few points, shown in Fig. 2(b). This allows us to constrain the Debye temperature $\theta(\rho)$ of the liquid independently of the melt curve $T_{\text{melt}}(P)$ at low densities.

Most of the available data pertaining to the liquid in the compression region lie at intermediate densities in the range up to about 22 g/cm^3 along the principal Hugoniot. Through an iterative process, we simultaneously fit $F_{\text{cold}}(\rho)$ and $\gamma_{\text{ion}}(\rho)$ of the liquid to the following set of data that reside in this range:

(1) The liquid branch of the principal Hugoniot, which starts at a pressure of about 2.6 Mbar [71] and is depicted in Figs. 3(c) and 3(d).

(2) As apparent from Figs. 3(c) and 3(d), there are significant regions that are notably devoid of Hugoniot data. In some of the regions that are sparse in data (particularly $14 \text{ g/cm}^3 < \rho < 15.2 \text{ g/cm}^3$, and $16 \text{ g/cm}^3 < \rho < 18 \text{ g/cm}^3$), we use our own DFT-MD simulations presented in Sec. III and Appendix A to help constrain the EOS. In addition, we consider the general insight of Wallace [139] that for elemental metals, ΔS_{melt} is $\sim 0.8 k_B/\text{atom}$. This finding has been used in the construction of other multiphase, high-pressure EOS models [141,155], and we use it to guide our

EOS development as well, along with the constraint from the reported ambient-pressure ΔS_{melt} value [4] of $1.04 k_B/\text{atom}$. To be clear, the DFT–MD simulations and this rule-of-thumb from Wallace are not hard constraints that we follow precisely; rather, they provide starting points from which we began our liquid EOS construction, and have helped to guide us as we gradually refine the model through the iterative process.

(3) For $P < 1.6$ Mbar, we fit to the DAC $T_{\text{melt}}(P)$ measurements of Anzellini *et al.* [29], which lie on the higher $T_{\text{melt}}(P)$ end. Considering Figs. 5(a) and 5(b) together, note that the difference, $F_{\text{cold}}^{\text{liquid}}(\rho) - F_{\text{cold}}^{\epsilon}(\rho)$, together with the log-ratio, $3k_B \ln[\theta^{\text{liquid}}(\rho)/\theta^{\epsilon}(\rho)]$, represent the internal energy difference and entropy difference, respectively, needed for the $T_{\text{melt}}(P)$ curve of our EOS to agree with our choice of Anzellini *et al.* [29] for $P < 1.6$ Mbar.

(4) For the intermediate pressures of 2–3 Mbar, there is an additional experimental constraint from the shock-melt measurements of Nguyen and Holmes [71].

(5) For 4 Mbar $< P < 10$ Mbar, we use the recent experiments of Kraus *et al.* [85] to inform our choice of T_{melt} . As described in more detail below, we use the phase identifications of Kraus *et al.* determined by *in situ* time-resolved x-ray diffraction as input for this choice.

Once $F_{\text{cold}}(\rho)$ and $\gamma_{\text{ion}}(\rho)$ in this intermediate density range are established in an iterative manner to agree with these data, we perform a numerical interpolation to connect these functions to their values at the near-ambient densities described in the preceding paragraph. We now take the next few paragraphs to explain in more detail how we have used some of the constraints listed above to determine $F_{\text{cold}}(\rho)$ and $\gamma_{\text{ion}}(\rho)$ of the liquid for $\rho < 22 \text{ g/cm}^3$, and then proceed to a discussion of how we determine $F_{\text{cold}}(\rho)$ and $\gamma_{\text{ion}}(\rho)$ of this phase at extreme densities up toward 10^3 g/cm^3 .

By measuring the abrupt changes in Lagrangian sound speed on the Hugoniot and associating said changes with the loss of strength in the liquid, Nguyen and Holmes [71] determined the intersection between the Hugoniot and solidus to be at 2.25 ± 0.03 Mbar, and the intersection with the liquidus to be at 2.60 ± 0.03 Mbar. These intersections provide tight constraints on the relationship between the four functions $F_{\text{cold}}^{\epsilon}(\rho)$, $F_{\text{cold}}^{\text{liquid}}(\rho)$, $\theta^{\epsilon}(\rho)$, and $\theta^{\text{liquid}}(\rho)$ in this restricted range. Figure 1(b) shows the results of this fitting, over the larger range of $0 < P < 4$ Mbar. $T_{\text{melt}}(P)$ is indicated by the boundary between gray (ϵ) and orange (liquid) regions. The dashed red curve shows our model’s prediction of the principal Hugoniot in T vs P , while the vertical red lines mark the pressures of intersection with solidus and liquidus boundaries as determined by Nguyen and Holmes (including their experimentally reported uncertainties) [71]. Too small or too large values of ΔV_{melt} and ΔS_{melt} at T_{melt} would give rise to a solid–liquid mixed-phase region on the Hugoniot that is either substantially smaller or larger than our present value. In the above analysis, we have assumed that a discontinuity in the slope of the experimentally determined longitudinal sound speed, $dC_L(P)/dP$, is exactly coincident with the pressure at which the Hugoniot intersects $T_{\text{melt}}(P)$. This may not be true in all cases, as argued by Beason *et al.* in recent work on other materials [176]. Likewise, recent work on shock melting by Turneure *et al.* [82] using *in situ* x-ray diffraction supports

a more complex picture [which is perhaps not surprising, given that detecting the inception of melting (where the phase fraction of liquid is very small) or completion of melting (very small phase fraction of solid) using x-ray techniques that probe the surface of a sample is a difficult task], where the width of the hcp–liquid, two-phase region on the principal Hugoniot is reported to be only 0.05 Mbar, which is significantly narrower than the 0.35 Mbar width observed from Nguyen and Holmes [71], and the approximately 0.24 Mbar width from DFT simulations. Although it is encouraging that the two-phase region from Turneure *et al.* resides within the middle of the 2.25 to 2.60 Mbar two-phase region from Nguyen and Holmes, suggesting at least some consistency between the two studies, we do not use Turneure *et al.* results to construct our EOS since they imply a rather small ΔV_{melt} (and correspondingly small ΔS_{melt}) that we do not expect Fe to exhibit. Brown and McQueen [52] also report shock-melting data along the principal Hugoniot. Their two-phase region resides within that of Nguyen and Holmes, though it is wider than the two-phase region reported by Turneure *et al.* [82]. But the sample involved in Brown and McQueen is actually a high-purity ($\sim 99\%$ Fe) steel, and not pure Fe like in Nguyen and Holmes. Although the steel sample is likely to behave similarly to pure Fe, the possible effect of the impurities on melting has not been well characterized above ambient pressure (although the melt temperature of the steel at ambient pressure is known to be lower than that of pure Fe), which is again why we have chosen Nguyen and Holmes to anchor the baseline versions of our EOS.

At the time of this writing, there is only one set of experimental data pertaining specifically to the Fe melt curve for $P > 4$ Mbar: In a 2022 study by Kraus *et al.* [85], samples of high-purity Fe were shocked to pressures between approximately 2 and 3 Mbar, and were then (following a brief release) ramp compressed to peak stresses between 5 and 10 Mbar. In each of the seven reported shots, *in situ* time-resolved x-ray diffraction was obtained during the ramp compression, and phase information was returned. Figures 7(a) and 7(b) display the final stresses (x axis) reached after the shock–ramp compression, indicated by the symbols. Attached to each is a dashed curve representing the isentrope corresponding to the ramp-compression path, as computed from our EOS. In the figure’s key, the phase identification at the peak stress from the x-ray diffraction [85] is listed, with “hcp”, “L”, and “mix” indicating pure-phase hcp, pure-phase liquid, and an hcp–liquid mixed phase, respectively. We have chosen here to interpret these particular phase identifications as representing *thermodynamic equilibrium* information [177], and this then prompts us to locate our model’s melt line to be that shown as the solid black curve in Fig. 7. It is crucial to stress that this constitutes a *particular assumption* regarding their measurements. That is, we have assumed that the solidification kinetics is sufficiently fast that the melt boundary, so determined, is not representative of a *metastable* (i.e., overdriven) extension of the liquid phase. While arguments put forth in Kraus *et al.* indicate that exceedingly rapid solidification is a distinct possibility, one may have to reassess this aspect of our multiphase EOS if further information inconsistent with this equilibrium assumption becomes available. (The melt curve would have to be shifted to higher

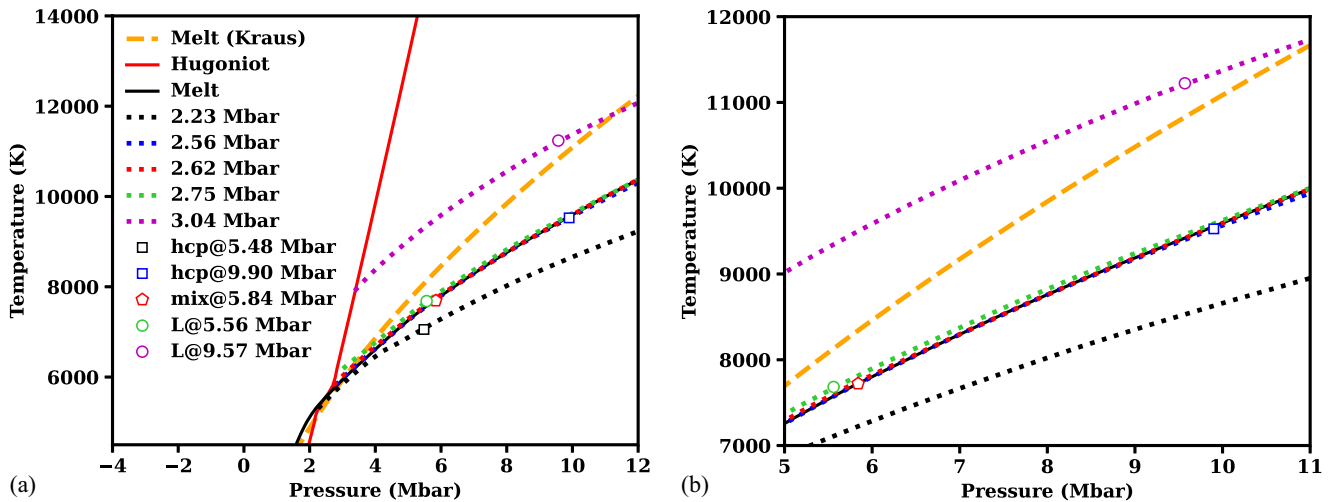


FIG. 7. (a) Principal Hugoniot (red curve), isentropes (dotted curves), and melt line (black curve) from our $\min-T_{\text{melt}}$ -SRX model together with the melt line inferred in a recent 2022 study by Kraus *et al.* [85] (orange curve). Here, we have analyzed five sets of shock-ramp experiments from their study. The pressures listed next to the labels for each isentrope (2.23–3.04 Mbar) indicate the pressures along the Hugoniot where each isentrope (i.e., the ramp portion of the experiments) was initiated. The open symbols represent the final stresses (5.48–9.90 Mbar) reached in the shock-ramp experiments, and they are colored to match those of their corresponding isentropes. Furthermore, the shapes of these symbols are such that the squares (\square), circles (\circ), and pentagon (\diamond) denote final experimentally accessed states that Kraus *et al.* determined via *in situ* x-ray diffraction to be in the hcp, liquid, and mixed (hcp + liquid) phases, respectively. The temperatures at which they cross the isentropes are determined by the $\min-T_{\text{melt}}$ -SRX version of our EOS model. (b) Magnified view of (a), concentrating on 5 Mbar < P < 11 Mbar.

temperatures in that case.) Under this equilibrium assumption, Kraus *et al.* additionally developed models to obtain estimates of the temperature/entropy along the melt curve and along the various shock-release paths. Their resulting $T_{\text{melt}}(P)$ curve, which is shown as the orange curve in Fig. 7, is still nevertheless different from our melt curve—even though we have used their experimental diffraction data on the phase identifications—because their underlying assumptions/models in estimating the melt temperatures are different from those of the free-energy models in our multiphase EOS. We discuss this in greater depth below in Sec. VB, where we construct model variations in an attempt to better understand these differences. The results of this analysis lead to EOS model uncertainties, which allow for a range of acceptable $T_{\text{melt}}(P)$ for $P > 5$ Mbar (see Fig. 13) and our two different EOS baseline models that capture this range.

At elevated pressures, there is a paucity of temperature measurements with which we can validate the thermal components of our Fe EOS. In recent years, however, experimental techniques have emerged to address this, and while they are still in development, we now present comparisons with these data (many of which pertain to the solid phases discussed above; we include these comparisons in this section because some pertain to the liquid phase). Figure 8 shows the Yoo *et al.* optical pyrometry-derived Hugoniot temperature [67] (right-facing triangles), the Brantley *et al.* optical pyrometry data (open squares) [83], and EXAFS (extended x-ray absorption fine structure; upward-facing triangles) data points along the principal Hugoniot (red), as well as various reshock states (blue). In the latter, *in situ* identification of the hcp crystal structure was also obtained. Note that while the EXAFS measurements on the Hugoniot [75], the solid-phase Hugoniot pyrometry data [83], and the liquid-phase pyrom-

etry measurements of Yoo *et al.* [67] are all in good accord with our model’s $T(P)$ Hugoniot, the optical pyrometry point from Brantley *et al.* [83] (open square at $P \sim 2.3$ Mbar) in

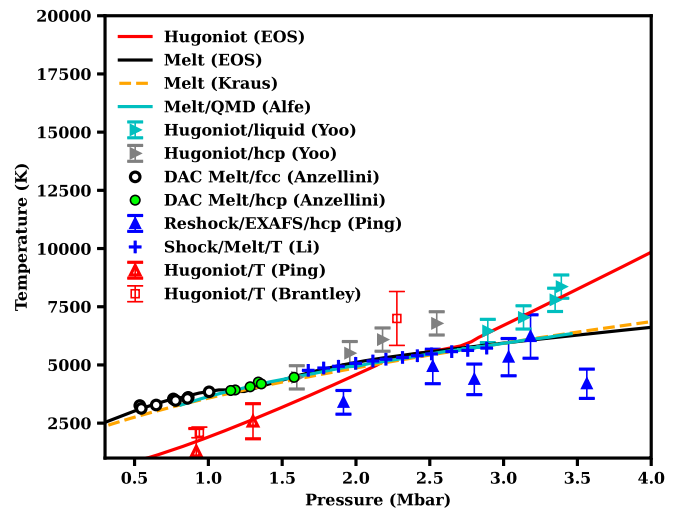


FIG. 8. Melt curve of our EOS (black line) together with that model’s principal Hugoniot (red line). Also shown are DAC measurements of $T_{\text{melt}}(P)$ from Anzellini *et al.* [29], fits of $T_{\text{melt}}(P)$ from the shock-melt inference of Li *et al.* [129] (blue + symbols), the shock-ramp melt inference reported in Kraus *et al.* [85] (orange dashed line), and Hugoniot temperature measurements from Yoo *et al.* [67] (gray and cyan right-pointing triangles). EXAFS (extended x-ray absorption fine structure) [75] and optical pyrometry [83] on Hugoniot and reshock states are represented by the upward-pointing triangular and square symbols, respectively, along with their reported error bars.

the liquid (also ostensibly on the principal Hugoniot) is in *disagreement* with our model. We do not have an explanation for the discrepancy at this time; we have chosen to keep our liquid free-energy model as-is despite this, due to our agreement with other experimental data in this range and DFT–MD predictions (Sec. III and Appendix A). In contrast, the lower- P pyrometry point from Brantley *et al.*, which lies at $P \sim 0.95$ Mbar in the ϵ phase, is quite close to our $T(P)$ Hugoniot, while the solid-phase Hugoniot temperature measurements of Yoo *et al.* [67] (gray right-facing triangles) are in marked disagreement with our model and other measurements [75,83]. Another high- T , high- P experimental inference is the entropy along the Fe Hugoniot as determined in a 2015 study by Kraus *et al.* [41], in which the authors connected ambient-pressure measurements of entropy at the vaporization point to a point on the Hugoniot at $P \sim 5$ Mbar through an assumed isentropic release. The entropy along the principal Hugoniot from our EOS, which was not fit to agree with this entropy inference, happens to go right through this point, providing further validation for our liquid Fe free-energy model. This experimental entropy point is lower than the values reported in the more recent 2022 study by Kraus *et al.* [85], which is reflected in the fact that our EOS yields lower melt temperatures than those inferred in the 2022 study, as illustrated in Fig. 7. Kraus *et al.* attribute the discrepancy in the 2015 and 2022 results to a difference in the reference entropy at a pressure of about 2.6 Mbar along the Hugoniot.

No experimental data on the thermophysical properties of Fe exist at the time of this writing for $\rho > 22$ g/cm³ (maximum density of the available principal Hugoniot data). We mentioned in Secs. II B and IV B that our liquid and solid $F_{\text{cold}}(\rho)$ functions asymptote to that of the PURGATORIO model [138] of Fe at high ρ , by construction, and that $\lim_{\rho \rightarrow \infty} \gamma_{\text{ion}}(\rho)$ is taken to be equal [159] to 1/2. These we deem to be proper choices. An approach to the prediction of the ionic-excitation contribution of Fe at ultrahigh compressions that is consistent with these choices is the work of Swift *et al.* [128], which used an extension [150] of the INFERNO model [137] to compute the density-dependent ionic Grüneisen parameter of Fe by invoking an Einstein vibrational model [139] within a spherical-atom-in-jellium context. We use these *ab initio* electronic-structure predictions of $\gamma_{\text{ion}}(\rho)$ to constrain our liquid (and ϵ phase) $\gamma_{\text{ion}}(\rho)$ functions for $\rho > 150$ g/cm³. This, together with an application of a Lindemann melt hypothesis [178] to set the trajectory of $T_{\text{melt}}(\rho)$ at these highest ρ , guarantees that our model's $T_{\text{melt}}(P)$ is of the same order of magnitude as the prediction of Swift *et al.* [128] in the many-TPa regime. Our $F_{\text{cold}}(\rho)$ and $\gamma_{\text{ion}}(\rho)$ functions from below 22 g/cm³ are connected to their values in this ultrahigh-density regime ($\rho > 150$ g/cm³) through numerical interpolation.

It is interesting to note that the Cell model [136,157] portion of our liquid free energy, described in Sec. II B, legislates a particular manner in which the ideal-gas limit is approached. More specifically, the precise evolution of $E_{\text{ion}}(\rho, T)$ and $P_{\text{ion}}(\rho, T)$ as T is raised above $T_{\text{melt}}(P)$ depends on our choice of $\theta^{\text{liquid}}(\rho)$. We previously examined this for the case of elemental Be [136] by comparing to high- T Kohn–Sham DFT–MD predictions of EOS. We hope to conduct a similar study for Fe in the future, to fully assess the implications of

our choices in this paper, *vis a vis* high- T liquid EOS. For now, we are at least satisfied that the shock data at all compressions is fit quite well by our liquid free-energy model, and that the $T \rightarrow \infty$ limit of our model is correct for both $E(\rho, T)$ and $P(\rho, T)$.

2. Expansion region: Liquid–vapor transition

For the low- ρ portion of our liquid EOS model, we construct a liquid–vapor transition region, as was also done by Kerley [133] and Medvedev [134] for their Fe EOS models. We choose to fit to the recent DFT–MD predictions of Li *et al.* [129], where the critical point was predicted to lie between 9000–9325 K in temperature and between 1.85–2.40 g/cm³ in density. To affect a liquid–vapor dome, we first join our previously constrained $F_{\text{cold}}^{\text{liquid}}(\rho)$ at higher densities to the form shown as the dashed line in Fig. 9(a). This creates a situation in which the energy of homogeneously expanded Fe in the dilute limit of an ideal gas becomes ρ independent, as required, and where the energy difference between $F_{\text{cold}}^{\text{liquid}}(\rho \rightarrow 0)$ and $F_{\text{cold}}(\rho_0) (\equiv E_0)$ is related to the cohesive energy. Such a cold internal-energy isotherm, otherwise uncorrected, would violate thermodynamic stability [139], because the resulting free energy would have the property, $(\partial^2 F / \partial V^2)_T < 0$. However, adding on a sensible thermal contribution and then requiring convexity of the total free energy leads to the familiar liquid–vapor transition [133,134,139,145,160].

The result of this construction for the low- ρ portion of $F_{\text{liquid}}(\rho, T)$, *prior* to enforcing convexity, is depicted in Fig. 9(b), showing pressure isotherms in the region of interest. The highest- T isotherm displayed (red curve) is one very near the critical isotherm; the precise (ρ, T) -location of the critical point was set by carefully adjusting the curvature of $F_{\text{cold}}^{\text{liquid}}(\rho)$ [Fig. 9(a)] in concert with the behavior of $\gamma_{\text{ion}}^{\text{liquid}}(\rho)$ in this regime.

In closing this Sec. IVE on the liquid, which is the last phase covered by our discussion on the EOS, we note that Appendix B contains parameters needed to construct analytic representations to portions of our phase-dependent free-energy models.

V. EOS MODEL VERSIONS MOTIVATED BY UNCERTAINTIES IN THE MELT DATA

A. Variation for $P < 3$ Mbar that addresses DAC melt uncertainties

As we have indicated variously throughout this paper, we choose to produce a *variation* to our multiphase Fe, which, unlike our baseline versions, respects agreement with the lower- $T_{\text{melt}}(P)$ values of Boehler *et al.* [26] and Sinmyo *et al.* [14]. Figure 10 shows the phase diagram of this variation of our EOS, which we refer to as low- T_{melt} -DAC, where we followed a nearly identical procedure to that outlined above, but with a different assumption for $T_{\text{melt}}(P)$. This phase diagram may be compared with that of our min- T_{melt} -SRX baseline model, which is shown in Fig. 1 and is fit to the higher $T_{\text{melt}}(P)$ inference from Anzellini *et al.* [29] for $P < 3$ Mbar.

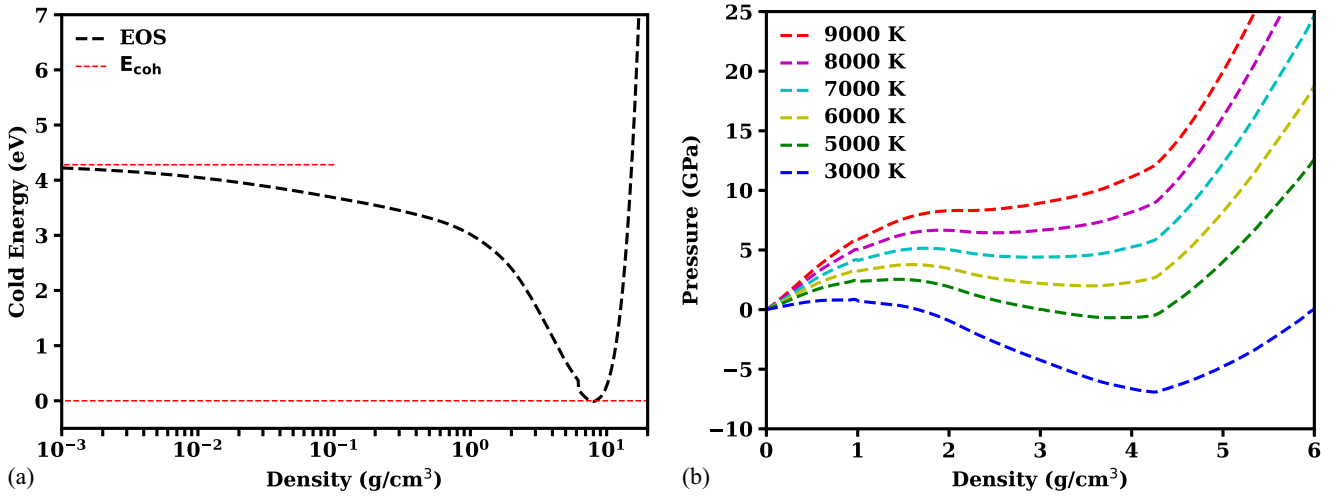


FIG. 9. (a) Cold curve, $F_{\text{cold}}(\rho)$ for the liquid in expansion. The vertical distance between the two red horizontal dashed lines indicates the cohesive (i.e., atomization) energy E_{coh} . (b) Pressure isotherms from the EOS, prior to a Maxwell construction, in the liquid–vapor transition regime. This nonconvex version of the EOS is required by many of the continuum, multiphysics codes [179–181] that are ubiquitous in high-energy-density science. In regions where the EOS returns a negative pressure, material damage/spall models in these codes come into play and override the EOS, thereby avoiding thermodynamic-stability issues that would otherwise be encountered. The convex version of the EOS, which can be obtained through a Maxwell construction, generates the liquid–vapor dome and the critical point, which are necessary for some of the applications discussed in Sec. VI.

Relative to the min- T_{melt} -SRX baseline model, the solid-phase free energies of the low- T_{melt} -DAC variation are very nearly the same, while the liquid model is more dissimilar. This is seen in Figs. 11(a) and 11(b), which present cold curves and Debye temperatures for the hcp and liquid phases of each EOS version. At the time of this writing, we have been unable to find a lower- T_{melt} parametrization, which preserves agreement with the Nguyen and Holmes shock-melt data [71], as illustrated in Fig. 10(b). Because we deem the Nguyen and Holmes data to be an important and reliable set of constraints, we have chosen our two baseline models (min- T_{melt} -SRX and max- T_{melt} -SRX; see Table I) to satisfy the high- T DAC melt line [29] so that they can also be consistent

with Nguyen and Holmes, and it is these two baseline versions that we recommend for use in planetary-modeling efforts. We designate our low- T_{melt} -DAC variation to represent an alternative scenario where one instead follows the DAC-derived melt line from Boehler *et al.* [26] and Sinmyo *et al.* [14] at the expense of not satisfying Nguyen and Holmes. We note, however, that the full swath of P vs ρ shock Hugoniot data points (as presented in Fig. 3) are fit equally well by both versions, given that these Hugoniot curves are essentially the same, as shown in Fig. 11(c). This reflects the fact that melt curves (and phase boundaries in general) tend to be more sensitive to free-energy variations than are Hugoniot curves.

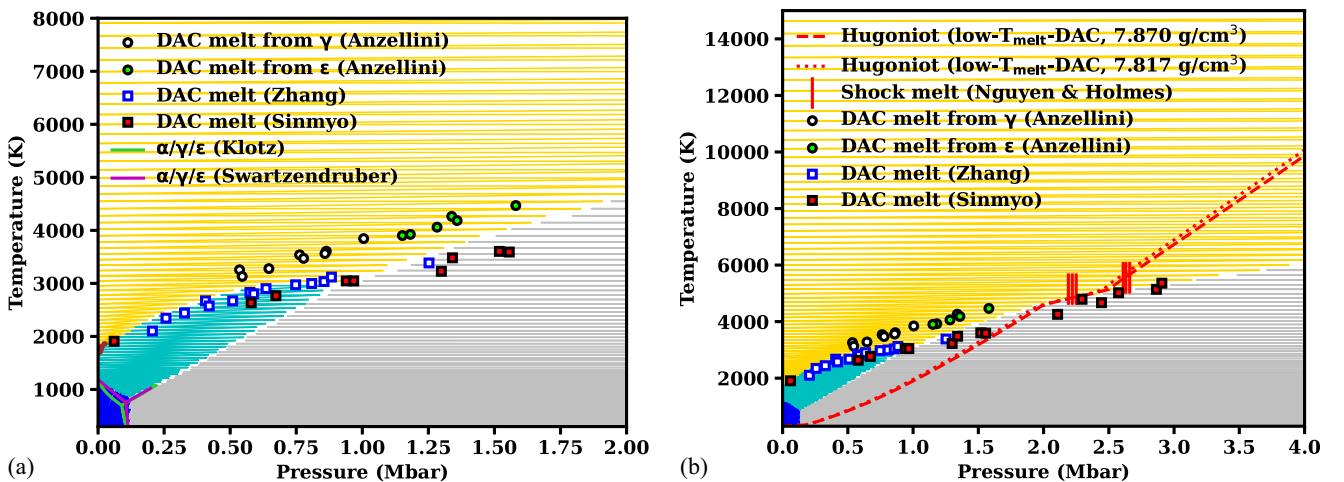


FIG. 10. Fe phase diagram for the low- T_{melt} -DAC variation of our multiphase EOS for pressures up to: (a) 2 Mbar, and (b) 4 Mbar. Blue indicates α , gray indicates ϵ , cyan indicates γ , and orange indicates the liquid. Also displayed are various points from experimental determinations of the melt curve.

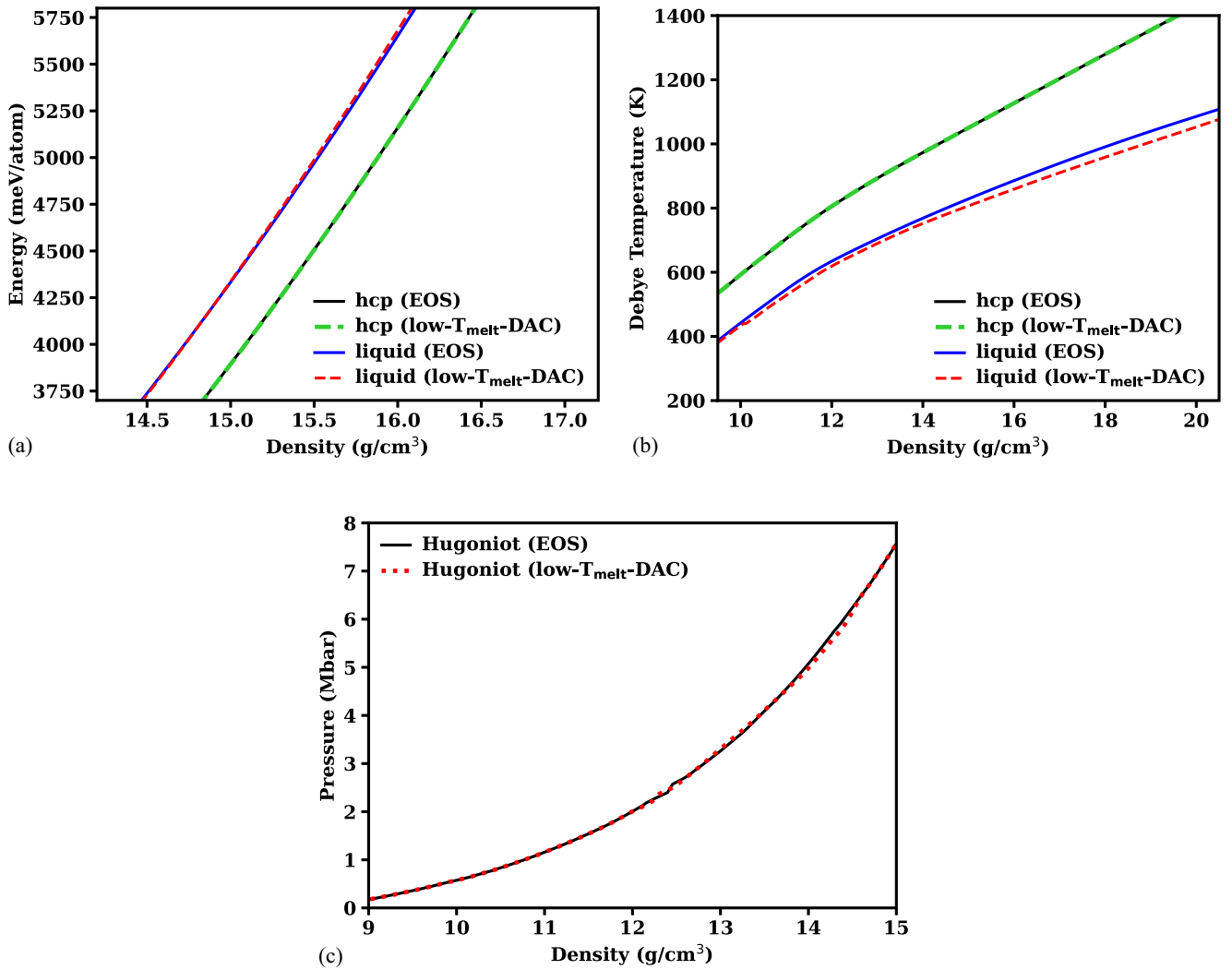


FIG. 11. Comparison of our baseline EOS (min- T_{melt} -SRX, which uses high- T DAC melt data) with our low- T_{melt} -DAC variation: (a) cold curves $F_{\text{cold}}(\rho)$ for the hcp (ϵ) and liquid phases; (b) Debye temperatures $\theta(\rho)$ for the hcp and liquid phases of both EOS versions; (c) P vs ρ along the principal Hugoniot.

B. Variations and baseline models that address melt-curve uncertainties at $P > 5$ Mbar in shock-ramp recrystallization experiments

In the discussion surrounding Fig. 7, we described the manner in which we used the Kraus *et al.* [85] *in situ* x-ray phase identification of Fe in their shock-ramp experiments to constrain the inputs to our liquid free-energy model in the 5 Mbar $< P < 10$ Mbar range. And while that discussion concerned the fitting of our baseline EOSs, it is clear that the nature of these data admit the possibility of a family of EOS models that all lead to similar agreement with these experimental phase identifications. In this section, we explore the space spanned by this family of EOSs (resulting in the baseline models: min- T_{melt} -SRX and max- T_{melt} -SRX), and create an additional EOS model variation (Kraus- T_{melt} -SRX) that exactly follows the Kraus *et al.* melt curve.

First, we stress that when we attempt to exactly follow the $T_{\text{melt}}(P)$ reported by Kraus *et al.* [85], we obtain an EOS model that predicts final states for two of their shock-(assumed isentropic) ramp experiments that are inconsistent

with their x-ray diffraction phase identifications. This is illustrated in Fig. 12, where the orange dashed line (which is nearly coincident with the solid black line) shows $T_{\text{melt}}(P)$ from Kraus *et al.*, and the red and green dashed lines show our model's isentropes emanating from shocked states with pressures of 2.62 Mbar and 2.75 Mbar, respectively. The open symbols with the corresponding colors indicate the final ramped pressures in these two shock-ramp experiments. The green pentagon is located within the solid-liquid mixed-phase region for any reasonable choice of EOS model inputs that are consistent with both our functional forms assumed in Sec. II, and the remaining thermophysical data for Fe that we have employed throughout Sec. IV. However, this final state was determined by the experiments to reside solely in the liquid [85]. Likewise, the red square is located in a pure (hcp) solid-phase region in our modeling, while the diffraction data showed clear signatures of an hcp-liquid mixed phase. It is for this reason that we are forced to explore a range of $T_{\text{melt}}(P)$ curves that deviate from the one reported by Kraus *et al.*

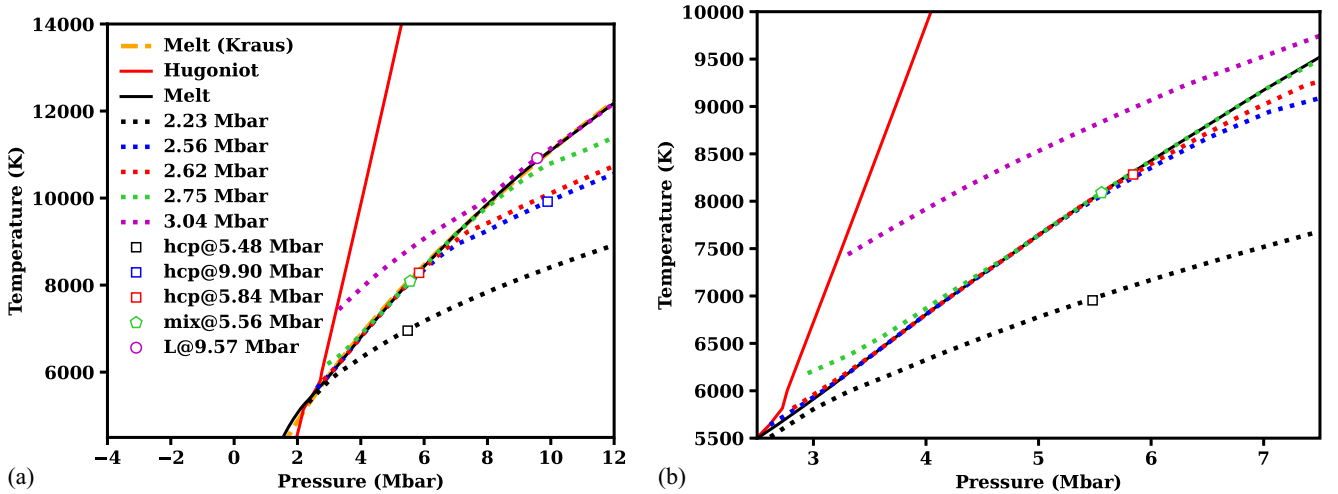


FIG. 12. (a) Principal Hugoniot (red curve), isentropes (dotted curves), and melt line (black curve) from our Kraus- T_{melt} -SRX model, which is the particular variation of our EOS that is designed to reproduce $T_{\text{melt}}(P)$ from Kraus *et al.* (the latter is depicted by the orange dashed curve). The open symbols located on each isentrope represent the final stresses (x axis) reached in various shock-ramp experiments reported in Kraus *et al.* [85]. The temperatures at which they cross the isentropes are determined by the Kraus- T_{melt} -SRX variation of our EOS. (b) Magnified view of (a).

Our strategy will be to identify, within the rubric of our free-energy models, both the highest and the lowest $T_{\text{melt}}(P)$ curves that are consistent with the x-ray-determined phase identifications reported by Kraus *et al.* [85], and in so doing, produce the EOS models described in Sec. IV: min- T_{melt} -SRX and max- T_{melt} -SRX. Starting from these baseline models, this assessment involves making the smallest possible modifications to $F_{\text{cold}}^{\text{liquid}}(\rho)$, $\theta^{\text{liquid}}(\rho)$, $F_{\text{cold}}^{\epsilon}(\rho)$, and $\theta^{\epsilon}(\rho)$ such that (1) the 9.90 Mbar final state (which is achieved by ramp compression from a 2.56 Mbar Hugoniot state) lies *just* within the pure ϵ (hcp) phase (min- T_{melt} version), and (2) the 9.57 Mbar final state (3.04 Mbar Hugoniot state) lies *just* within the pure liquid phase (max- T_{melt} version). In both limiting cases, as with all intermediate model choices, the 5.84 Mbar final state (2.62 Mbar Hugoniot state) is mandated to lie within the ϵ -liquid mixed-phase region, and the 5.56 Mbar final state (2.75 Mbar Hugoniot state) is constrained to lie in the pure liquid phase. These limiting cases are displayed, in a manner identical to that of Fig. 7, in Fig. 13(a) for min- T_{melt} -SRX and Fig. 13(b) for max- T_{melt} -SRX. Combining these limiting $T_{\text{melt}}(P)$ curves from our analysis with the $T_{\text{melt}}(P)$ determination and error estimates reported in Kraus *et al.* [85], we arrive at the plot shown in Fig. 14. The Kraus *et al.* melt curve lies above that from our max- T_{melt} -SRX model above 4 Mbar (both curves by design agree with Anzellini *et al.* [29] below this pressure range). However, we note that our max- T_{melt} does partly lie in the uncertainty estimates presented by Kraus *et al.* [85], which is indicated by the fact that the gray shaded region between our max- T_{melt} and min- T_{melt} possesses a small, but notable overlap with the magenta shaded region between the dashed curves in Fig. 14.

The fact that there is an overlap in our respective $T_{\text{melt}}(P)$ uncertainty estimates is encouraging. However, the fact that these regions are mostly nonoverlapping (for $P > 6$ Mbar), despite both analyses utilizing the same shock-(assumed isentropic) ramp experiments, highlights the substantive differences in the two approaches when translating these

final-state pressures to final-state temperatures. The assumptions leading to our final-state temperature predictions are embodied in the free-energy models that we have employed (see Sec. II), together with the phase-dependent fitting of these models (see Secs. IV B and IV E) using a host of experimental data, including the x-ray diffraction data from Kraus *et al.* As described in the Supplemental Material that accompanies their paper [85], Kraus *et al.* infer $T_{\text{melt}}(P)$ by employing a model that utilizes several experimentally constrained/inferred quantities of the liquid phase: the heat capacity C_V , Grüneisen parameter γ , adiabatic sound speed C_S on the Hugoniot, principal Hugoniot $P(\rho)$ and $T(\rho)$, and principal isentrope $P(\rho)$. They use their model to perform a thermodynamic integration to arrive at melt temperatures. It is therefore insightful to exhibit these same quantities as rendered in our EOS model in an effort to understand why our melt temperatures tend to be lower than theirs.

Figure 15 illustrates these relevant quantities. We see from Fig. 15(a) that our thermodynamic Grüneisen parameter γ is smaller than that of Kraus *et al.* [85]. The figure also includes direct experimental inferences on γ from two studies. The red squares represent results in the liquid from Brown and McQueen [52], while the black squares are a reanalysis performed by Anderson and Ahrens [182] on the Brown and McQueen results. To the extent of our knowledge, these are the only direct experimental inferences that have been reported on liquid γ in the relevant density range. We note that γ in our EOS is a function of temperature (as well as density) because of the contribution from the electron-thermal term, but the temperature dependence is fairly weak for the conditions shown in Fig. 15(a) so that our γ curve at 10 000 K is only slightly above the 6000 K γ curve depicted in the figure. Kraus *et al.* constrain their Grüneisen parameter—which they treat as a function of density only—with sound-speed C_S measurements from Nguyen and Holmes [71] and the pressure-density relation along the principal Hugoniot reported by Brown *et al.* [57], Fig. 15(b) reveals that our EOS

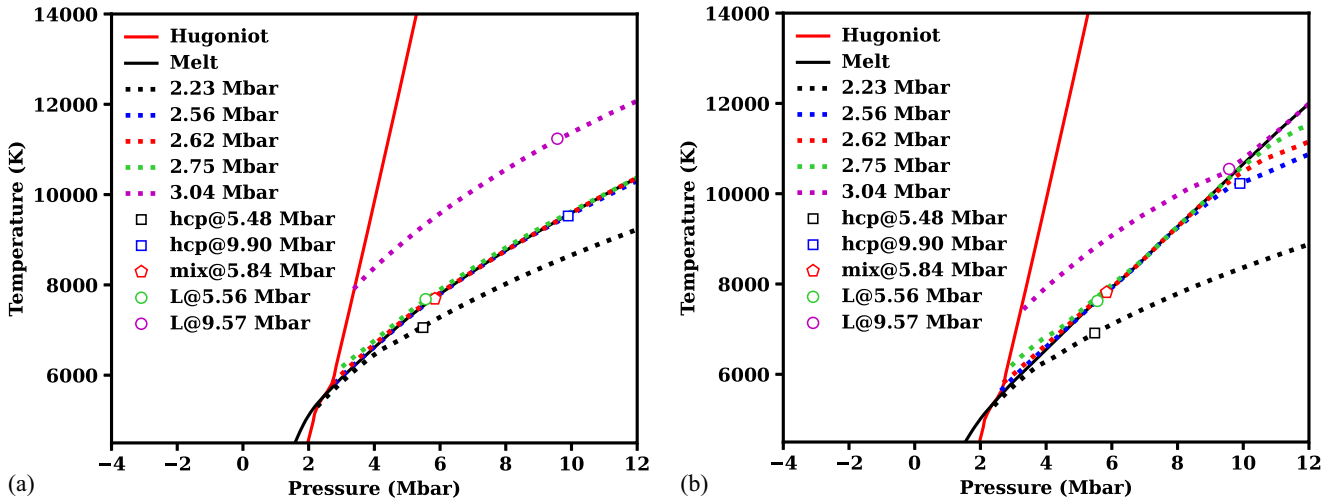


FIG. 13. (a) Principal Hugoniot (red curve), isentropes (dashed curves), and melt line (black curve) from our min- T_{melt} -SRX model. The open symbols located on each isentrope represent the final stresses (x axis) reached in various shock-ramp experiments reported in Kraus *et al.* [85]. The temperatures at which they cross the isentropes are determined by the min- T_{melt} -SRX version of our EOS model. (b) Same as (a), but for the max- T_{melt} -SRX version of our EOS.

also agrees well with C_s from Nguyen and Holmes. It is worth pointing out that these C_s data were not used as constraints to our free-energy models, and so the good agreement gives some confidence in the true predictive capabilities of our EOS. (For completeness, we note that Brown and McQueen also report C_s data along the Hugoniot, but we have not included their results in the figure because the material involved in their study is actually a high-purity steel, and not pure Fe like in Nguyen and Holmes, as we have mentioned earlier.) We

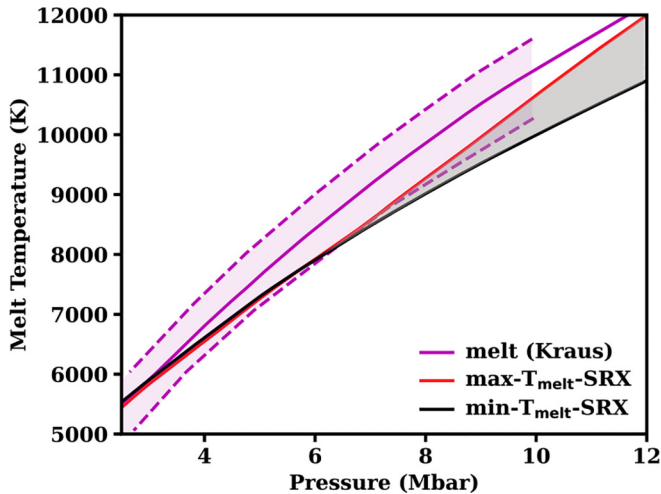


FIG. 14. Lower-bound (solid black) and upper-bound (solid red) melt curves from our EOS models, where we have colored the region between these two curves in gray. These curves come from our min- T_{melt} -SRX and max- T_{melt} -SRX models, respectively. Analytical fits of the melt curves from these two models to the Simon-Glatzel equation in the range 0–15 Mbar are given in Appendix B. They are plotted alongside the $T_{\text{melt}}(P)$ curve reported by Kraus *et al.* [85] (solid magenta) and the uncertainty bounds on $T_{\text{melt}}(P)$ presented in that work (dashed magenta curves that envelope the magenta shaded region).

have utilized data from Brown *et al.* [57], as well as many other sources, to constrain the liquid-phase EOS, as shown in Fig. 3(c) and 3(d). Switching our focus now to the heat capacity C_V , Fig. 15(c) indicates that our C_V is generally higher than the value of $4.2 k_B/\text{atom}$ (with uncertainties of $\pm 1.0 k_B/\text{atom}$) Kraus *et al.* used to perform their analysis. Interestingly, despite the somewhat large differences in C_V , our relative entropy along the Hugoniot agrees well with what Kraus *et al.* have obtained [Fig. 15(d)], and there are not dramatic differences in the relative entropies along the liquidus and solidus curves either [Fig. 15(e)]. Nevertheless, the higher C_V in our case is consistent with our arrival at lower melt temperatures, and we again point the reader to Fig. 8, which demonstrates that our EOS accurately predicts Hugoniot temperatures since the data in the figure serve as holdouts that were not fit to our EOS. In order to infer the melt temperature from their experimental data, Kraus *et al.* follow a two-step thermodynamic path in which one of these steps involves performing a thermodynamic integration over an isentrope. More specifically, this step involves integration of the liquid-phase γ , which is an isentropic logarithmic derivative of temperature with respect to density, along an isentrope where the two limits of integration are (1) the $\sim 12.5 \text{ g/cm}^3$ density at the liquidus/Hugoniot intersection point and (2) the density of the point along the liquidus whose T_{melt} we are trying to determine. The latter is where Fig. 15(f), which compares the P - ρ behavior along the liquidus in our EOS with that assumed by Kraus *et al.*, comes into play. One can see from the figure that our liquidus has a lower ρ for a given P (i.e., is stiffer). Therefore, if the same thermodynamic integration procedure as in Kraus *et al.* were performed but with quantities computed from our EOS instead, one would end up integrating smaller values of γ over a narrower density range and would thus arrive at a lower T_{melt} than that reported in their study. In summary, the smaller γ and liquidus density, along with the higher C_V , are the main reasons why our $T_{\text{melt}}(P)$ tends to lie below $T_{\text{melt}}(P)$ from Kraus *et al.*, as portrayed in Fig. 14.

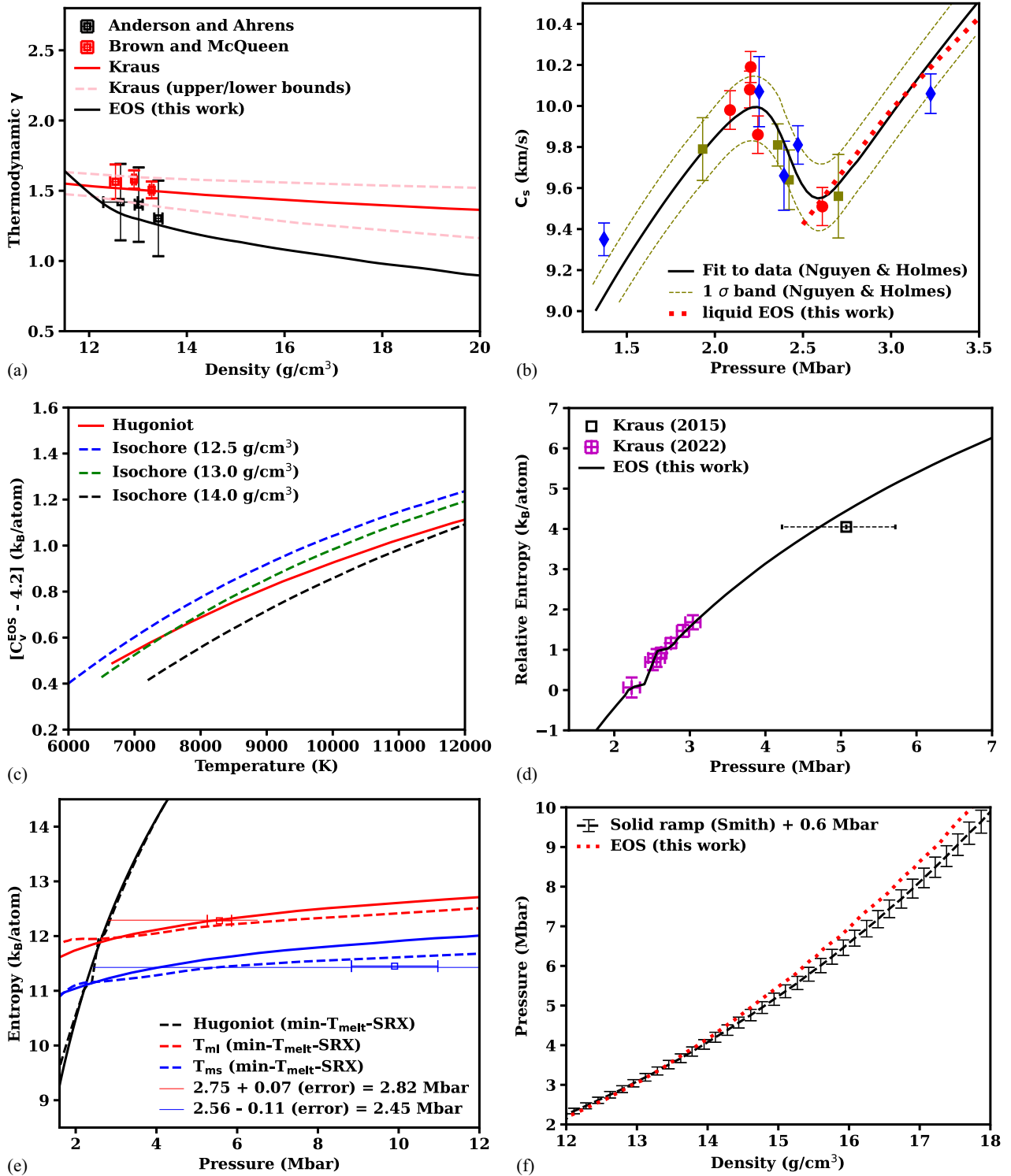


FIG. 15. Liquid-phase quantities of interest in determining $T_{\text{melt}}(P)$: (a) Thermodynamic Grüneisen parameter γ from our EOS (along the 6000 K isotherm) compared with γ of the Kraus *et al.* model [85] and representative experimental data [57,182]. (b) Sound speed C_s data reported by Nguyen and Holmes [71] vs predictions in the liquid from our EOS. (c) Heat capacity C_V from our EOS minus the 4.2 k_B/atom value assumed by Kraus *et al.* [85]. (d) Entropy along the principal Hugoniot, which is plotted relative to the entropy value at the solidus/Hugoniot intersection (which occurs at around 2.25 Mbar) [71]. An earlier value reported by Kraus *et al.* [41] in 2015 is also included. (e) Entropy along the Hugoniot, liquidus (T_{ml}), and solidus (T_{ms}) in our min- T_{melt} -SRX model, all of which are depicted by dashed curves, compared against those same curves from Kraus *et al.* (see the solid lines), which we have shifted by $-1.08 k_B/\text{atom}$ to align with our EOS at 2.6 Mbar (where the liquidus intersects the principal Hugoniot), as well as the two shock-ramp data points (with error bars) reported by Kraus *et al.* that provide the strongest constraints on the melt curve. (f) P vs ρ along the liquidus in our EOS and Kraus' model, the latter of which involves adding a 0.6 Mbar pressure correction to the ramp-compression curve of Smith *et al.* [42].

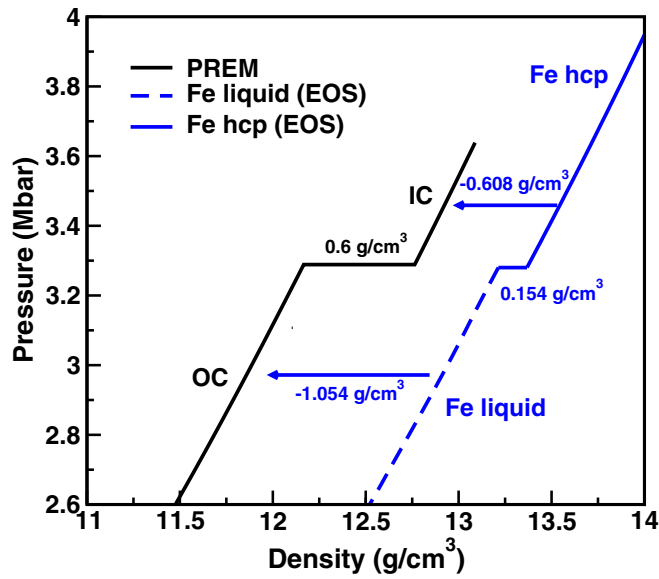


FIG. 16. Pressure-vs-density isentropes for the Earth's ICB from the Preliminary Earth Reference Model (PREM) study [112] (black) and from our EOS (blue).

VI. INITIAL GEOPHYSICAL AND PLANETARY-SCIENCE APPLICATIONS OF THE EOS

As we stated at the outset, precise knowledge of the multiphase Fe EOS is needed for the modeling of planetary interiors, particularly those which are broadly similar to Earth in size. One topic of perennial interest is a more accurate and nuanced understanding of the nature of Earth's core, and specifically the thermodynamic conditions of the inner-core boundary (ICB). In a recent experimental work, Li *et al.* [81] attempted to infer the temperature at the ICB from measurements of the shock-melt temperature of Fe using *in situ* optical pyrometry during dynamic compression with a two-stage gas gun. After a lengthy analysis, they arrived at the estimate $T_{\text{melt}}(P_{\text{ICB}} = 3.28 \text{ Mbar}) = 5990 \text{ K}$, largely in agreement with the DAC inference of Anzellini *et al.* [29] and the gas-gun + pyrometry work of Yoo *et al.* [67], but in disagreement with the more recent pyrometry work of Brantley *et al.* [83], in which a much higher shock temperature was inferred. The min- T_{melt} -SRX baseline model gives $T_{\text{melt}}(P = 3.28 \text{ Mbar}) = 5975 \text{ K}$, quite close to the Li *et al.* work. We therefore submit that the present Fe EOS will likely be of use to planetary scientists aimed at exploring questions pertaining to Earth's interior, provided that they are interested in doing so while respecting some of these recent experimental inferences [29,81].

Also of interest is the density at the ICB and the associated density difference $\Delta\rho \equiv \rho_{\text{IC}} - \rho_{\text{OC}}$ between Earth's inner and outer cores, which are primarily composed of solid and liquid Fe, respectively. Figure 16 shows isentropes from our EOS model (blue), which exhibits a liquid \rightarrow hcp transition as ρ is increased. The black curve shows the inferences of these same IC and OC densities from the PREM (Preliminary Reference Earth Model) study [112], in which the density determinations were made after careful examination of seismic data. Both black and blue isentropes have the

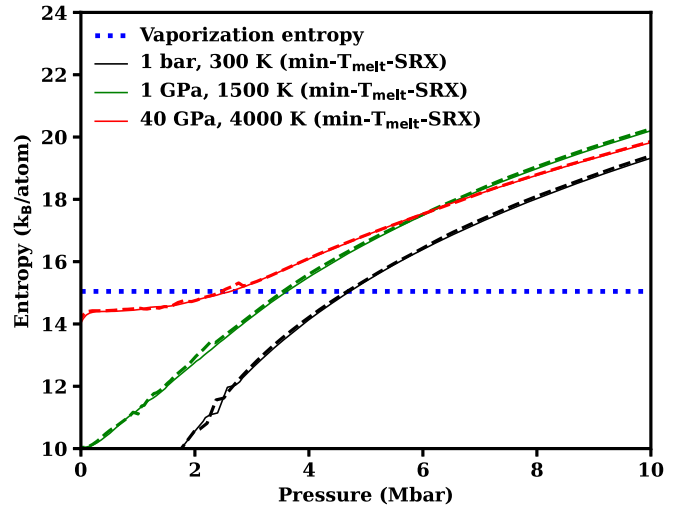


FIG. 17. Entropy along three different loci of shock Hugoniot, each corresponding to a different initial condition. Solid curves indicate the results of our min- T_{melt} -SRX baseline EOS model, while dashed curves indicate the results of our low- T_{melt} -DAC variation. The horizontal dotted blue line marks the entropy of vaporization [41].

transition pressure at 3.28 Mbar (by design), but there is a notable disagreement in both the value of $\Delta\rho$ (PREM's 0.6 g/cm^3 vs our baseline model's 0.154 g/cm^3), and the absolute density values. This has been discussed before in the context of other Fe EOS models, and is known as the *density deficit*. If this deficit is sizable, as it is in the case of the comparison between our EOS model and PREM, it strongly suggests that the composition of Earth's core should have significant contributions from lighter elements (such as Ni, S, Si, O, C, H) [112]. Indeed, the larger density deficit exhibited by the outer core could indicate that these lighter impurities are more soluble in the liquid than in the solid. Further analysis with our family of Fe EOS models, as employed in studies of the EOSs of mixtures of Fe with other elements and the associated phase-equilibria calculations (such as those performed in one of our recent studies [183]) may prove enlightening in this regard. In such cases, it may be necessary to consider the possibility of a thermodynamically stable high-pressure bcc phase, if such an allotrope is established to be favored for cases of Fe mixed with other elements.

Finally, the Fe EOS is central to the study of Earth-core vaporization due to giant impacts, such as might have occurred to create our Moon [184]. In modeling this phenomenon, it is crucial for the Fe EOS to contain a description of the liquid-vapor transition (as ours does; see Sec. IVE 2), and it is of interest to examine the pressure at which Fe vaporization occurs, from which one can then predict how much Fe vapor is likely to be released from the core during a given impact event. Figure 17 shows the entropy along the shock Hugoniot, as computed from our EOS model, from several different initial conditions, as discussed in the planetary-collision scenarios considered in Li *et al.* [81]. In Fig. 17, we have taken the vaporization entropy to be $\sim 15 \text{ k}_B/\text{atom}$; this leads to specific vaporization pressures represented by the crossings ($\sim 2 \text{ Mbar}$, 3.5 Mbar , and 4.5 Mbar) for the

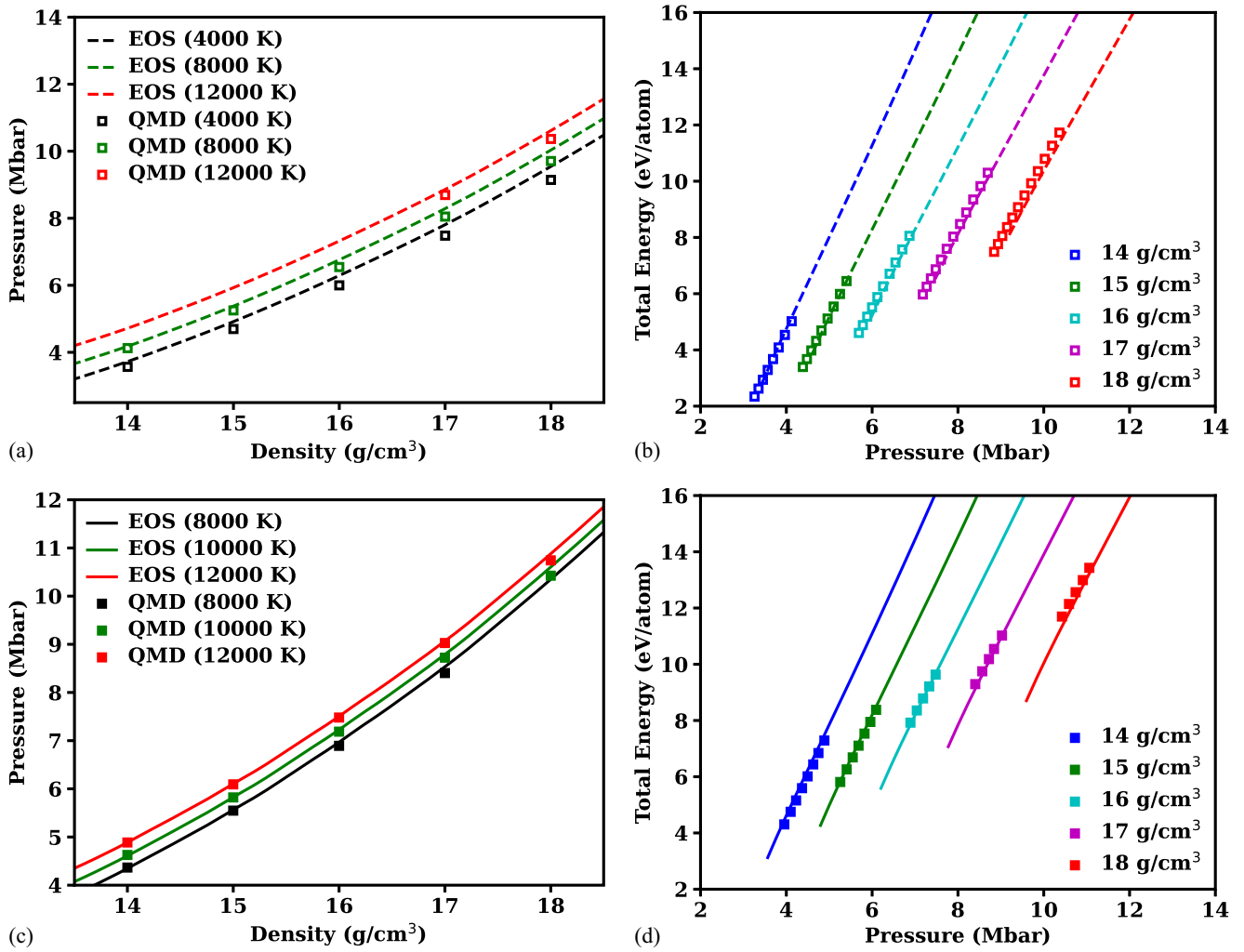


FIG. 18. Comparisons between DFT-MD and our (baseline) EOS model for the ϵ (hcp) phase: (a) $P(\rho, T)$, (b) $E(\rho, P)$. Open squares are the DFT-MD predictions for the hcp phase, and the dashed lines are from the hcp EOS model. Comparisons between DFT-MD and the EOS model for the liquid phase: (c) $P(\rho, T)$, (d) $E(\rho, P)$. Squares are the DFT-MD predictions for the liquid phase, and the solid lines are from the liquid EOS model.

different scenarios. It is also worth noting that the two high- T_{melt} -DAC models (i.e., the two baseline versions) and the low- T_{melt} -DAC variation of our Fe EOS all possess nearly the same shock-vaporization pressures, as shown in Fig. 17. We suspect that our Fe EOS models will prove useful in future planetary-impact studies.

VII. CONCLUSIONS

We have presented the construction of a wide-ranged, five-phase equation of state for elemental iron, in which ambient-pressure, low-pressure, and static as well as dynamic high-pressure experimental data were used to fit our phase-specific free-energy models. We have designed this Fe EOS to be accurate for planetary-science and high-pressure applications, including those relevant to ICB conditions and planetary evolution and collision scenarios [41]. To achieve this goal, we focus our EOS development on five key areas: (1) compressibility, (2) shock-and-release behavior, (3) high-pressure

melting, (4) thermal expansion, and (5) vaporization with a sensible liquid-vapor dome region. The resulting multiphase EOS is designed to fit a diverse and carefully selected set of data that span several orders of magnitude in temperature and density. Furthermore, the EOS also demonstrates strong predictive capability by providing excellent agreement with certain holdout data not used in the EOS fitting. Specifically, we have demonstrated good agreement with (1) solid-phase [75,83] and liquid-phase [67] Hugoniot temperature measurements (Fig. 8); (2) liquid sound-speed measurements [71] along the principal Hugoniot [Fig. 15(b)]; and (3) isentropic release-wave profiles from an elevated temperature condition [Fig. 6(b)], all of which further demonstrate the fidelity of our models.

Construction of the EOS requires addressing EOS data for certain key properties that have been the subject of persistent (and sometimes contentious) disagreement in the literature. In particular, there are disagreements in: (1) the DAC $T_{\text{melt}}(P)$, and (2) the presence or absence of a stable high-pressure bcc

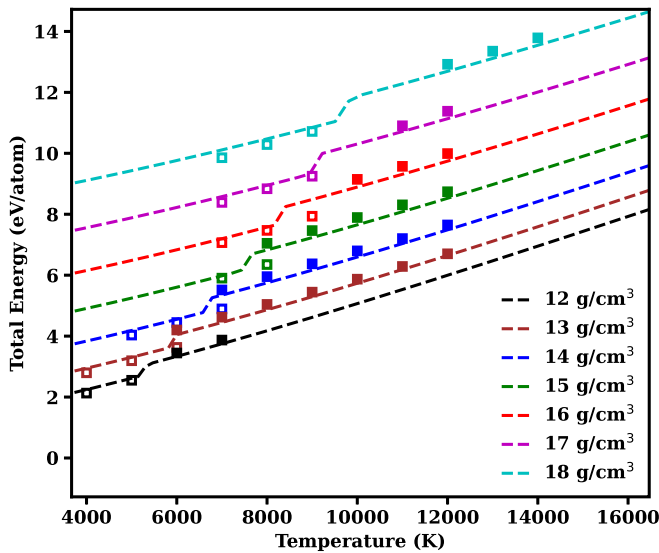


FIG. 19. Comparison with DFT–MD for the total energy of both hcp and the liquid along isochores that collectively span a range of 12–18 g/cm³. Symbols are the DFT–MD predictions, and solid lines are from the EOS model. See text for details.

phase. We have responded to the first of these disagreements by constructing separate *variations* to appease the two melt scenarios while keeping EOS constraints that are deemed reasonably accurate unchanged (see Table II). This enables us to assess the likelihood of each scenario by analyzing how well the different EOS versions agree with other high-fidelity experimental data or observations. Using this EOS-variation-consistency approach, we conclude that the high- T_{melt} -DAC curve [29,81] is more likely to be correct because it is only this branch that is consistent with shock-melting measurements [71]. It is for this reason that the high- T_{melt} -DAC data are selected and incorporated into our baseline models.

At higher pressures, we have paid special attention to the results of the recent multi-Mbar shock-ramp measurements (SRX) published by Kraus *et al.* [85] in which solidification was detected using x-ray diffraction techniques at pressures between 5–10 Mbar. Since the temperature along the SRX compression path was not directly measured, Kraus *et al.* employed a thermodynamic model to infer the melt temperature from their data [85]. We have analyzed all seven of their SRX shots and have found that above 6 Mbar, there is significant ambiguity associated with the possible melt temperatures: namely, there exists not one, but a family of EOS models—whose melt curves are bounded by the min- T_{melt} -SRX and max- T_{melt} -SRX versions depicted in Fig. 14—that all satisfy the required agreement with SRX recrystallization phase observations. We find that our resulting melt curves must end up being lower than that of Kraus *et al.*, although these melt curves do overlap partly with the uncertainty bounds reported in their study. We anticipate that there will be many SRX experiments in the future aimed at providing further constraints on the melt above 6 Mbar, and one recommendation we make for such studies is to take x-ray images around 9.5 Mbar for a series of closely spaced ramp-compression paths initiated from shocked states near where the two-phase region along

the principal Hugoniot is thought to reside (say, between 2.55–2.75 Mbar).

In the mean time, it is our hope that our multiphase EOS will be useful in addressing the sensitivities and uncertainties for various planetary-science applications like further improving our understanding of the interior structure, evolution, and formation of Earth and super-Earth planets. Furthermore, in addition to applications in planetary science, our Fe EOS can be used to construct EOS models for other iron-rich materials of industrial relevance, such as stainless steels.

ACKNOWLEDGMENTS

We thank R. G. Kraus, P. Söderlind, J. L. Belof, J. H. Eggert, D. C. Swift, H. Shelton, and S. D. Crockett for many helpful discussions. This work was performed under the auspices of the US Department of Energy under Contract No. DE-AC52-07NA27344.

APPENDIX A: DFT–MD RESULTS FOR THE EOS OF HIGH-PRESSURE Fe

Here we present our VASP (16-valence-electron) PAW pseudopotential DFT–MD results [161–168] (see Tables III and IV), computed according to the specifications outlined in Sec. III. Figures 18(a) and 18(b) show P vs ρ along three isotherms, and E vs P along five isochores, both for the hcp phase. Points indicate DFT–MD predictions, while the curves display the results of our EOS model. Agreement is quite good overall, though there are systematic discrepancies at the lowest temperature (for P), and at the higher densities (and lower E) for the $E(P)$ relationship. Figures 18(c) and 18(d) show plots of the same quantities, but for the liquid phase. Figure 19 portrays the internal energy of our multiphase EOS model as a function of T for five isochores, along with the DFT–MD predictions for both hcp (open squares) and the liquid (filled squares). The signatures of the melt transition in both the *ab initio* predictions and the EOS model are quite apparent, manifesting in jumps in E as T is increased. We emphasize that direct input from *ab initio* predictions of $T_{\text{melt}}(P)$ and $(\Delta V_{\text{melt}}, \Delta S_{\text{melt}})$ was avoided in the creation of the EOS model; for instance, we let the width of the shock-melt region as determined experimentally by Nguyen and Holmes [71] dictate the magnitudes of ΔV_{melt} and ΔS_{melt} in our EOS. Rather, as mentioned in Secs. IV E and III, we have used the *ab initio* simulations to provide starting points from which we began our liquid-phase EOS construction and to help guide the further refinement of our multiphase EOS in certain regions of thermodynamic state space where available data are absent.

APPENDIX B: EOS PARAMETERS

Here, we present parameters and associated functional forms which describe our underlying free-energy models. Table V shows the parameters of a localized fit of our cold energy and cold pressure near the ambient density ρ_0 to empirical model forms (Vinet or AP2), where E_0 , B_0 , and B' are the energy, bulk modulus, and pressure derivative of the bulk

TABLE III. DFT–MD isochores for hcp (ϵ -phase) Fe. See Sec. III for details regarding the computational methodology and associated parameters.

ρ (g/cm ³)	T (K)	P (GPa)	E (kJ/g)
12.0	1000.0	150.96	-14.24
12.0	2000.0	159.69	-13.73
12.0	3000.0	169.61	-13.15
12.0	4000.0	180.84	-12.49
12.0	5000.0	193.40	-11.76
13.0	1000.0	230.45	-13.02
13.0	2000.0	239.43	-12.53
13.0	3000.0	249.41	-11.97
13.0	4000.0	260.63	-11.34
13.0	5000.0	272.84	-10.66
13.0	6000.0	286.42	-9.90
14.0	1000.0	325.90	-11.51
14.0	2000.0	335.20	-11.02
14.0	3000.0	345.39	-10.47
14.0	4000.0	356.65	-9.87
14.0	5000.0	368.98	-9.20
14.0	6000.0	382.19	-8.49
14.0	7000.0	396.60	-7.72
14.0	8000.0	412.47	-6.88
15.0	1000.0	438.52	-9.69
15.0	2000.0	447.96	-9.20
15.0	3000.0	458.28	-8.67
15.0	4000.0	469.58	-8.08
15.0	5000.0	481.92	-7.44
15.0	6000.0	496.17	-6.71
15.0	7000.0	510.26	-5.97
15.0	8000.0	525.08	-5.20
15.0	9000.0	540.29	-4.41
16.0	1000.0	569.05	-7.59
16.0	2000.0	578.37	-7.11
16.0	3000.0	588.55	-6.59
16.0	4000.0	599.82	-6.02
16.0	5000.0	612.23	-5.39
16.0	6000.0	625.46	-4.73
16.0	7000.0	640.81	-3.96
16.0	8000.0	654.45	-3.27
16.0	9000.0	670.37	-2.46
16.0	10 000.0	687.02	-1.63
17.0	1000.0	718.08	-5.23
17.0	2000.0	727.08	-4.75
17.0	3000.0	737.02	-4.24
17.0	4000.0	748.13	-3.69
17.0	5000.0	760.42	-3.08
17.0	6000.0	773.78	-2.43
17.0	7000.0	789.03	-1.68
17.0	8000.0	804.96	-0.90
17.0	9000.0	819.37	-0.19
17.0	10 000.0	835.64	0.60
17.0	11 000.0	852.63	1.43
17.0	12 000.0	869.47	2.25
18.0	1000.0	884.30	-2.61
18.0	2000.0	893.36	-2.14
18.0	3000.0	903.29	-1.64
18.0	5000.0	926.73	-0.50
18.0	6000.0	940.02	0.13
18.0	7000.0	955.17	0.86

TABLE III. (Continued.)

ρ (g/cm ³)	T (K)	P (GPa)	E (kJ/g)
18.0	8000.0	970.69	1.60
18.0	9000.0	986.39	2.35
18.0	10 000.0	1002.33	3.10
18.0	11 000.0	1019.42	3.91
18.0	12 000.0	1036.61	4.71

TABLE IV. DFT–MD isochores for liquid Fe. See Sec. III for details regarding the computational methodology and associated parameters.

ρ (g/cm ³)	T (K)	P (GPa)	E (kJ/g)
12.0	4000.0	201.91	-11.60
12.0	5000.0	213.41	-10.92
12.0	6000.0	225.46	-10.22
12.0	7000.0	237.22	-9.50
12.0	8000.0	248.82	-8.79
13.0	4000.0	284.37	-10.35
13.0	5000.0	296.78	-9.66
13.0	6000.0	311.09	-8.88
13.0	7000.0	322.74	-8.19
13.0	8000.0	335.10	-7.48
14.0	5000.0	395.30	-8.11
14.0	6000.0	410.01	-7.34
14.0	7000.0	422.77	-6.64
14.0	8000.0	436.59	-5.89
14.0	9000.0	449.65	-5.16
14.0	10 000.0	462.71	-4.43
14.0	11 000.0	474.81	-3.73
14.0	12 000.0	488.67	-2.96
15.0	6000.0	525.66	-5.51
15.0	7000.0	540.70	-4.73
15.0	8000.0	554.75	-4.00
15.0	9000.0	568.31	-3.28
15.0	10 000.0	582.18	-2.53
15.0	11 000.0	595.80	-1.82
15.0	12 000.0	609.25	-1.07
16.0	8000.0	689.23	-1.86
16.0	9000.0	704.10	-1.11
16.0	10 000.0	718.66	-0.37
16.0	11 000.0	733.11	0.37
16.0	12 000.0	747.98	1.09
17.0	8000.0	840.35	0.51
17.0	9000.0	856.75	1.29
17.0	10 000.0	872.25	2.04
17.0	11 000.0	884.06	2.67
17.0	12 000.0	902.67	3.49
18.0	10 000.0	1042.40	4.66
18.0	11 000.0	1058.85	5.43
18.0	12 000.0	1074.28	6.15
18.0	13 000.0	1091.03	6.90
18.0	14 000.0	1106.19	7.65

TABLE V. Parameters for the fits of the cold curve of different phases in our EOS to the Vinet and Holzzapfel AP2 [185] models at near-ambient pressures.

Phase	Model	E_0 (meV/atom)	B_0 (GPa)	B'	ρ_0 (g/cm ³)	Fitting Range
bcc (α)	Vinet	0	164.8	5.55	7.927	7.5–8.5 g/cm ³
fcc (γ)	Vinet	69.5	152.7	6.81	8.018	7.5–8.5 g/cm ³
bcc (δ)	Vinet	79.7	153.2	6.52	7.949	7.5–8.5 g/cm ³
hcp (ϵ)	AP2	40.3	180.7	5.28	8.373	7.5–9.5 g/cm ³
liquid	AP2	160.5	147.6	7.82	8.027	7.5–8.5 g/cm ³

modulus, respectively, at ρ_0 (or $V_0 = 1/\rho_0$). Table VI presents a fit of the Debye temperature to a polynomial in the specified density range. The Holzzapfel AP2 model [185] employs the following form for the cold pressure as a function of volume:

$$P_{\text{cold,AP2}}(x) = 3B_0 \left(\frac{1-x}{x^5} \right) \exp [a_0(1-x)][1 + a_2x(1-x)], \quad (\text{B1})$$

where $x = (V/V_0)^{1/3}$, $a_0 = -\ln(3B_0/P_{\text{FGr}})$, $a_2 = (3/2)(B' - 3) - a_0$, $P_{\text{FGr}} = a_{\text{FG}}(Z/V_0)^{5/3}$, Z is the atomic number, and the Fermi gas parameter $a_{\text{FG}} = 0.02337 \times 10^{-25}$ (erg/cm³) cm⁵. The corresponding expression for the cold energy [186] as a function of volume is

$$F_{\text{cold,AP2}}(x) = E_0 + \frac{9V_0B_0}{2x^2} \exp [a_0(1-x)] \times \left[1 - \left(a_0 + 2 - 2a_2 \frac{2+a_0}{a_0} \right) x \text{FE}(a_0x) - 2x \frac{a_2}{a_0} (2-x) \right], \quad (\text{B2})$$

where $\text{FE}(y)$ is defined as the following product of an exponential integral with an exponential function,

$$\text{FE}(y) = 1 - y \exp(y) \int_y^{100} \frac{\exp(-z)}{z} dz, \quad (\text{B3})$$

TABLE VI. Debye temperature as a function of density for five considered Fe phases, fitted over a limited range by polynomials: $\theta(\rho) = \sum_{k=0}^n c_k \rho^k$, with the coefficients c_k listed here.

Phase	c_0	c_1	c_2	c_3	c_4	Fitting Range
bcc (α)	-3076.38	781.433	-44.6498	-0.453593	0.0827836	8–12.0 g/cm ³
fcc (γ)	6616.4	-2346.05	305.114	-16.2672	0.307302	8–12.0 g/cm ³
bcc (δ)	14275.9	-5140.78	621.6	-24.6657	0	8–9.0 g/cm ³
hcp (ϵ)	5038	-1899	267.9	-15.54	0.3294	8–14.0 g/cm ³
liquid	8734.78	-3297.18	457.758	-26.8967	0.579952	8–14.0 g/cm ³

which Holzzapfel approximates as

$$\text{FE}(y) \approx \frac{(y^2 + 2.334733y + 0.250621)}{(y^2 + 3.330657y + 1.681534)}. \quad (\text{B4})$$

The functional form for the Vinet model is

$$F_{\text{cold,Vinet}}(V) = E_0 + \frac{4V_0B_0}{(B'_0 - 1)^2} [1 - (1 + X) \exp(-X)], \quad (\text{B5})$$

in which $X = (3/2)(B'_0 - 1)[(V/V_0)^{1/3} - 1]$. Table VII presents our Simon–Glatzel fit to the melt curves for our two baseline models. These melt curves are depicted in Fig. 14.

APPENDIX C: EOS TABLE DETAILS

Our four multiphase Fe EOS models (the two baseline versions and two variations), are each defined over the range: 10^{-5} g/cm³ < ρ < 10^3 g/cm³, and 100 K < T < 10^9 K. Tables of discrete points in (ρ, T) are provided for the total internal energy E , the total pressure P , and the total entropy S . The ρ and T grid points are spaced logarithmically. The

TABLE VII. Melt curve for our two baseline Fe EOS models, min- T_{melt} -SRX and max- T_{melt} -SRX, fitted over a limited range by the Simon–Glatzel equation: $T_{\text{melt}}(P) = T_{\text{melt}}^{\text{ref}} \left(\frac{P - P^{\text{ref}}}{a} + 1 \right)^b \exp[-c(P - P^{\text{ref}})]$, with the fit parameters listed here. Here, P is the pressure in units of Mbar. The three solid phases that span the pressure range indicated in the table are δ (high-temperature bcc), γ (fcc), and ϵ (hcp). These melt curves are also illustrated graphically in Fig. 14.

Model	$T_{\text{melt}}^{\text{ref}}$	P^{ref}	a	b	c	Fitting range
min- T_{melt} -SRX	1811.0	0.0	0.2121	0.4308	0.0	0–15.0 Mbar
max- T_{melt} -SRX	1811.0	0.0	0.1764	0.3759	-0.0244	0–15.0 Mbar

resolution of the (ρ, T) grid is sufficiently fine to represent mixed-phase regions. Thermodynamic consistency, arising from the equality of mixed partial derivatives of the free energy [e.g., $(\partial P / \partial T)_\rho = -(\rho^2 / m_{\text{Fe}})(\partial S / \partial \rho)_T$], is assessed by using BIMOND interpolation [187] and finite-difference computations of the derivatives; we calculate that such conditions are accurately satisfied on all points with the exception of those in close proximity to phase transitions. This is to be expected, and we find that our tabular Fe EOS models are similar to other multiphase EOS tables we have recently made in this regard [136].

- [1] T. Saitō, Y. Shiraishi, and Y. Sakuma, *Trans. Iron Steel Inst. Jpn.* **9**, 118 (1969).
- [2] J. Brillo and I. Egry, *Z. Metallkd.* **95**, 691 (2004).
- [3] R. N. Abdullaev, R. A. Khairulin, and S. V. Stankus, *J. Phys.: Conf. Ser.* **1675**, 012087 (2020).
- [4] E. S. Domalski and E. D. Hearing, *NIST Chemistry WebBook*, edited by P. J. Linstrom and W. G. Mallard, Condensed Phase Heat Capacity data, in NIST Standard Reference Database Number 69; National Institute of Standards and Technology (NIST, Gaithersburg, MD., 2018), <https://webbook.nist.gov/chemistry>, retrieved 6/2021.
- [5] Q. Williams, R. Jeanloz, J. Bass, B. Svendsen, and T. J. Ahrens, *Science* **236**, 181 (1987).
- [6] H. K. Mao, Y. Wu, L. C. Chen, J. F. Shu, and A. P. Jephcoat, *J. Geophys. Res.* **95**, 21737 (1990).
- [7] C. S. Yoo, J. Akella, A. J. Campbell, H. K. Mao, and R. J. Hemley, *Science* **270**, 1473 (1995).
- [8] H.-R. Wenk, S. Matthias, R. J. Hemley, H.-K. Mao, and J. Shu, *Nature (London)* **405**, 1044 (2000).
- [9] L. S. Dubrovinsky, S. K. Saxena, F. Tutti, S. Rekhi, and T. LeBehan, *Phys. Rev. Lett.* **84**, 1720 (2000).
- [10] R. J. Hemley and H.-K. Mao, *Int. Geol. Rev.* **43**, 1 (2010).
- [11] D. Zhang, J. M. Jackson, J. Zhao, W. Sturhahn, E. E. Alp, M. Y. Hu, T. S. Toellner, C. A. Murphy, and V. B. Prakapenka, *Earth Planet. Sci. Lett.* **447**, 72 (2016).
- [12] P. I. Dorogokupets, A. M. Dymshits, K. D. Litasov, and T. S. Sokolova, *Sci. Rep.* **7**, 41863 (2017).
- [13] G. Morard, S. Boccato, A. D. Rosa, S. Anzellini, F. Miozzi, L. Henry, G. Garbarino, M. Mezouar, M. Harmand, F. Guyot, E. Boulard, I. Kantor, T. Irifune, and R. Torchio, *Geophys. Res. Lett.* **45**, 11074 (2018).
- [14] R. Sinmyo, K. Hirose, and Y. Ohishi, *Earth Planet. Sci. Lett.* **510**, 45 (2019).
- [15] R. L. Clendenen and H. G. Drickamer, *J. Phys. Chem. Solids* **25**, 865 (1964).
- [16] H.-K. Mao, W. A. Bassett, and T. Takahashi, *J. Appl. Phys.* **38**, 272 (1967).
- [17] A. P. Jephcoat, H. K. Mao, and P. M. Bell, *J. Geophys. Res.* **91**, 4677 (1986).
- [18] R. Boehler, *Nature (London)* **363**, 534 (1993).
- [19] S. K. Saxena, G. Shen, and P. Lazor, *Science* **264**, 405 (1994).
- [20] S. K. Saxena, L. S. Dubrovinsky, P. Häggkvist, Y. Cerenius, G. Shen, and H. K. Mao, *Science* **269**, 1703 (1995).
- [21] D. Andrault, G. Fiquet, M. Kunz, F. Visocekas, and D. Häuserman, *Science* **278**, 831 (1997).
- [22] D. Andrault, G. Fiquet, T. Charpin, and T. Le Bihan, *Am. Mineral.* **85**, 364 (2000).
- [23] S. K. Saxena and L. S. Dubrovinsky, *Am. Mineral.* **85**, 372 (2000).
- [24] A. Dewaele, P. Loubeyre, F. Occelli, M. Mezouar, P. I. Dorogokupets, and M. Torrent, *Phys. Rev. Lett.* **97**, 215504 (2006).
- [25] A. Dewaele, M. Torrent, P. Loubeyre, and M. Mezouar, *Phys. Rev. B* **78**, 104102 (2008).
- [26] R. Boehler, D. Santamaría-Pérez, D. Errandonea, and M. Mezouar, *J. Phys.: Conf. Ser.* **121**, 022018 (2008).
- [27] S. Tateno, K. Hirose, Y. Ohishi, and Y. Tatsumi, *Science* **330**, 359 (2010).
- [28] D. Yamazaki, E. Ito, T. Yoshino, A. Yoneda, X. Guo, B. Zhang, W. Sun, A. Shimojuku, N. Tsujino, T. Kunimoto, Y. Higo, and K. Funakoshi, *Geophys. Res. Lett.* **39**, L20308 (2012).
- [29] S. Anzellini, A. Dewaele, M. Mezouar, P. Loubeyre, and G. Morard, *Science* **340**, 464 (2013).
- [30] J. M. Jackson, W. Sturhahn, M. Lerche, J. Zhao, T. S. Toellner, E. E. Alp, S. V. Sinogeikin, J. D. Bass, C. A. Murphy, and J. K. Wicks, *Earth Planet. Sci. Lett.* **362**, 143 (2013).
- [31] T. Sakai, S. Takahashi, N. Nishitani, I. Mashino, E. Ohtani, and N. Hirao, *Phys. Earth Planet. Inter.* **228**, 114 (2014).
- [32] Y. Fei, C. Murphy, Y. Shibazaki, A. Shahar, and H. Huang, *Geophys. Res. Lett.* **43**, 6837 (2016).
- [33] A. Dewaele and G. Garbarino, *Appl. Phys. Lett.* **111**, 021903 (2017).
- [34] A. Dewaele, V. Svitlyk, F. Bottin, J. Bouchet, and J. Jacobs, *Appl. Phys. Lett.* **112**, 201906 (2018).
- [35] E. Boulard, C. Denoual, A. Dewaele, A. King, Y. L. Godec, and N. Guignot, *Acta Mater.* **192**, 30 (2020).
- [36] Y. Kuwayama, G. Morard, Y. Nakajima, K. Hirose, A. Q. R. Baron, S. I. Kawaguchi, T. Tsuchiya, D. Ishikawa, N. Hirao, and Y. Ohishi, *Phys. Rev. Lett.* **124**, 165701 (2020).
- [37] L. Dubrovinsky, N. Dubrovinskaia, and V. Prakapenka, *Física del la Tierra* **23**, 72 (2011).
- [38] L. Dubrovinsky, N. Dubrovinskaia, O. Narygina, I. Kantor, A. Kuznetsov, V. B. Prakapenka, L. Vitos, B. Johansson, A. S. Mikhaylushkin, S. I. Simak, and I. A. Abrikosov, *Science* **316**, 1880 (2007).
- [39] A. S. Balchan and G. R. Cowan, *J. Geophys. Res.* **71**, 3577 (1966).

- [40] R. Jeanloz, *J. Geophys. Res.* **84**, 6059 (1979).
- [41] R. G. Kraus, S. Root, R. W. Lemke, S. T. Stewart, S. B. Jacobsen, and T. R. Mattsson, *Nat. Geosci.* **8**, 269 (2015).
- [42] R. F. Smith, D. E. Fratanduono, D. G. Braun, T. S. Duffy, J. K. Wicks, P. M. Celliers, S. J. Ali, A. Fernandez-Pañella, R. G. Kraus, D. C. Swift *et al.*, *Nat. Astron.* **2**, 452 (2018).
- [43] R. G. McQueen and S. P. Marsh, *J. Appl. Phys.* **31**, 1253 (1960).
- [44] L. V. Al'tshuler, S. B. Kormer, A. A. Bakanova, and R. F. Trunin, *J. Exptl. Theoret. Phys. (U.S.S.R.)* **38**, 790 (1960) [*Sov. Phys. - JETP* **11**, 573 (1960)].
- [45] L. V. Al'tshuler, S. B. Kormer, M. I. Brazhnik, L. A. Vladimirov, M. P. Speranskaya, and A. I. Funtikov, *J. Exptl. Theoret. Phys. (U.S.S.R.)* **38**, 1061 (1960) [*Sov. Phys. - JETP* **11**, 766 (1960)].
- [46] L. V. Al'tshuler, A. A. Bakanova, and R. F. Trunin, *J. Exptl. Theoret. Phys. (U.S.S.R.)* **42**, 91 (1962) [*Sov. Phys. - JETP* **15**, 65 (1962)].
- [47] I. C. Skidmore and E. Morris, *International Atomic Energy Agency, Thermodynamics of Nuclear Materials*, International Atomic Energy Agency (IAEA, Vienna, 1962), p. 173.
- [48] K. K. Krupnikov, A. A. Bakanova, M. I. Brazhnik, and R. F. Trunin, *Sov. Phys. - Dokl.* **148**, 1302 (1963).
- [49] L. V. Al'tshuler, B. N. Moiseev, L. V. Popov, G. V. Simakov, and R. F. Trunin, *Zh. Eksp. Teor. Fiz.* **54**, 785 (1968) [*Sov. Phys. - JETP* **27**, 420 (1968)].
- [50] L. V. Al'tshuler and B. S. Chekin, *Proceed. of 1 All-Union Pulsed Pressures Symposium (VNIIFTRI, Moscow, 1974)* [in Russian] **1**, 5 (1974).
- [51] L. V. Al'tshuler, A. A. Bakanova, I. P. Dudoladov, E. A. Dynin, R. F. Trunin, and B. S. Cheki, *J. Appl. Mech. Tech. Phys.* **22**, 145 (1981).
- [52] J. M. Brown and R. G. McQueen, *J. Geophys. Res.: Solid Earth* **91**, 7485 (1986).
- [53] R. F. Trunin, M. A. Podurets, L. V. Popov, V. N. Zubarev, A. A. Bakanova, V. M. Ktitorov, A. G. Sevast'yanov, G. V. Simakov, and I. P. Dudoladov, *Zh. Eksp. Teor. Fiz.* **102**, 1433 (1992) [*Sov. Phys. - JETP* **75**, 777 (1992)].
- [54] R. F. Trunin, M. A. Podurets, B. N. Moiseev, G. V. Simakov, and A. G. Sevast'yanov, *Zh. Eksp. Teor. Fiz.* **103**, 2189 (1993) [*Sov. Phys. - JETP* **76**, 1095 (1993)].
- [55] R. F. Trunin, *Phys. Usp.* **37**, 1123 (1994).
- [56] L. V. Al'tshuler, R. F. Trunin, K. K. Krupnikov, and N. V. Panov, *Phys. Usp.* **39**, 539 (1996).
- [57] J. M. Brown, J. N. Fritz, and R. S. Hixson, *J. Appl. Phys.* **88**, 5496 (2000).
- [58] R. F. Trunin, L. F. Gudarenko, M. V. Zhernokletov, and G. V. Simakov, *Experimental Data on Shock Compression and Adiabatic Expansion of Condensed Matter*, edited by R. F. Trunin (RFNC-VNIIEF, Sarov, 2001).
- [59] D. Bancroft, E. L. Peterson, and S. Minshall, *J. Appl. Phys.* **27**, 291 (1956).
- [60] J. M. Walsh, M. H. Rice, R. G. McQueen, and F. L. Yarger, *Phys. Rev.* **108**, 196 (1957).
- [61] L. V. Al'tshuler, K. K. Krupnikov, B. N. Ledenev, V. I. Zhuchikhin, and M. I. Brazhnik, *J. Exptl. Theoret. Phys. (U.S.S.R.)* **34**, 874 (1958) [*Sov. Phys. - JETP* **7**, 606 (1958)].
- [62] R. G. McQueen, S. P. Marsh, J. W. Taylor, J. N. Fritz, and W. J. Carter, The equation of state of solids from shock wave studies, in *High Velocity Impact Phenomena*, edited by R. Kinslow (Academic Press, Cambridge, MA, 1970), pp. 293–417; appendixes on pp. 515–568.
- [63] L. M. Barker and R. E. Hollenbach, *J. Appl. Phys.* **45**, 4872 (1974).
- [64] L. V. Al'tshuler, N. N. Kalitkin, L. V. Kuz'mina, and B. S. Chekin, *Zh. Eksp. Teor. Fiz.* **72**, 317 (1977) [*Sov. Phys. - JETP* **45**, 167 (1977)].
- [65] C. E. Ragan, *Phys. Rev. A* **29**, 1391 (1984).
- [66] R. S. Hixson and J. N. Fritz, in *Shock Compression of Condensed Matter–1991*, edited by S. C. Schmidt, R. D. Dick, J. W. Forbes, and D. G. Tasker (Elsevier, Amsterdam, 1992) pp. 69–70.
- [67] C. S. Yoo, N. C. Holmes, M. Ross, D. J. Webb, and C. Pike, *Phys. Rev. Lett.* **70**, 3931 (1993).
- [68] M. V. Zhernokletov, G. V. Simakov, Y. N. Sutulov, and R. F. Trunin, *High Temp.* **33**, 36 (1995).
- [69] *High Pressure and High Temperature Equation-of-State of Gamma and Liquid Iron* (Springer Science and Business Media, New York, 1997), Vol. 499.
- [70] M. J. Brown, *Geophys. Res. Lett.* **28**, 4339 (2001).
- [71] J. H. Nguyen and N. C. Holmes, *Nature (London)* **427**, 339 (2004).
- [72] D. H. Kalantar, J. F. Belak, G. W. Collins, J. D. Colvin, H. M. Davies, J. H. Eggert, T. C. Germann, J. Hawreliak, B. L. Holian, K. Kadau, P. S. Lomdahl, H. E. Loranzana, M. A. Meyers, K. Rosolankova, M. S. Schneider, J. Sheppard, J. S. Stölken, and J. S. Wark, *Phys. Rev. Lett.* **95**, 075502 (2005).
- [73] J. A. Hawreliak, D. H. Kalantar, J. S. Stölken, B. A. Remington, H. E. Lorenzana, and J. S. Wark, *Phys. Rev. B* **78**, 220101(R) (2008).
- [74] J. Hawreliak, B. El-Dasher, H. Lorenzana, G. Kimminau, A. Higginbotham, B. Nagler, S. M. Vinko, W. J. Murphy, T. Whitcher, J. S. Wark, S. Rothman, and N. Park, *Phys. Rev. B* **83**, 144114 (2011).
- [75] Y. Ping, F. Coppari, D. G. Hicks, B. Yaakobi, D. E. Fratanduono, S. Hamel, J. H. Eggert, J. R. Rygg, R. F. Smith, D. C. Swift, D. G. Braun, T. R. Boehly, and G. W. Collins, *Phys. Rev. Lett.* **111**, 065501 (2013).
- [76] J. Wang, R. F. Smith, J. H. Eggert, D. G. Braun, T. R. Boehly, J. R. Patterson, P. M. Celliers, R. Jeanloz, G. W. Collins, and T. S. Duffy, *J. Appl. Phys.* **114**, 023513 (2013).
- [77] T. Sakaiya, H. Takahashi, T. Kondo, T. Kadono, Y. Hironaka, T. Irifune, and K. Shigemori, *Earth Planet. Sci. Lett.* **392**, 80 (2014).
- [78] N. Amadou, E. Brambrink, T. Vinci, A. Benuzzi-Mounaix, G. Huser, S. Brygoo, G. Morard, F. Guyot, T. de Resseguier, S. Mazevet *et al.*, *Phys. Plasmas* **22**, 022705 (2015).
- [79] M. Harmand, A. Ravasio, S. Mazevet, J. Bouchet, A. Denoëud, F. Dorchie, Y. Feng, C. Fourment, E. Galtier, J. Gaudin, F. Guyot, R. Kodama, M. Koenig, H. J. Lee, K. Miyanishi, G. Morard, R. Musella, B. Nagler, M. Nakatsutsumi, N. Ozaki *et al.*, and *Phys. Rev. B* **92**, 024108 (2015).
- [80] A. Denoëud, N. Ozaki, A. Benuzzi-Mounaix, H. Uranishi, Y. Kondo, R. Kodama, E. Brambrink, A. Ravasio, M. Bocoum, J. M. Boudenne *et al.*, *Proc. Natl. Acad. Sci. USA* **113**, 7745 (2016).
- [81] J. Li, Q. Wu, J. Li, T. Xue, Y. Tan, X. Zhou, Y. Zhang, Z. Xiong, Z. Gao, and T. Sekine, *Geophys. Res. Lett.* **47**, e2020GL087758 (2020).

- [82] S. J. Turneaure, S. M. Sharma, and Y. M. Gupta, *Phys. Rev. Lett.* **125**, 215702 (2020).
- [83] D. A. Brantley, R. S. Crum, and M. C. Akin, *J. Appl. Phys.* **129**, 015903 (2021).
- [84] S. C. Grant, T. Ao, C. T. Seagle, A. J. Porwitsky, J. P. Davis, K. R. Cochrane, D. H. Dolan, J. F. Lin, T. Ditmire, and A. C. Bernstein, *J. Geophys. Res.: Solid Earth* **128**, e2020JB020008 (2021).
- [85] R. G. Kraus, R. J. Hemley, S. J. Ali, J. L. Belof, L. X. Benedict, J. Bernier, D. Braun, R. E. Cohen, G. W. Collins, F. Coppari *et al.*, *Science* **375**, 202 (2022).
- [86] A. M. Dziewonski and F. Gilbert, *Nature (London)* **234**, 465 (1971).
- [87] R. Jeanloz and H.-R. Wenk, *Geophys. Res. Lett.* **15**, 72 (1988).
- [88] K. C. Creager, *Nature (London)* **356**, 309 (1992).
- [89] J. Tromp, *Nature (London)* **366**, 678 (1993).
- [90] L. Stixrude and R. E. Cohen, *Science* **267**, 1972 (1995).
- [91] L. Stixrude, E. Wasserman, and R. E. Cohen, *J. Geophys. Res.: Solid Earth* **102**, 24729 (1997).
- [92] A. Souriau and B. Romanowicz, *Phys. Earth Planet. Inter.* **101**, 33 (1997).
- [93] X. Song, *Rev. Geophys.* **35**, 297 (1997).
- [94] A. B. Belonoshko, R. Ahuja, and B. Johansson, *Phys. Rev. Lett.* **84**, 3638 (2000).
- [95] B. A. Buffett, *Science* **288**, 2007 (2000).
- [96] D. L. Anderson, *Proc. Natl. Acad. Sci. USA* **99**, 13966 (2002).
- [97] B. A. Buffett, *Science* **315**, 1801 (2007).
- [98] R. D. van der Hilst, M. V. de Hoop, P. Wang, S.-H. Shim, P. Ma, and L. Tenorio, *Science* **315**, 1813 (2007).
- [99] X. Sun and X. Song, *Earth Planet. Sci. Lett.* **269**, 56 (2008).
- [100] A. B. Belonoshko, T. Bryk, and A. Rosengren, *Phys. Rev. Lett.* **104**, 245703 (2010).
- [101] K. Hirose, S. Labrosse, and J. Hernlund, *Annu. Rev. Earth Planet Sci.* **41**, 657 (2013).
- [102] H. Tkalčić, *Rev. Geophys.* **53**, 59 (2015).
- [103] M. Mattesini, A. B. Belonoshko, E. Buforna, M. Ramírez, S. I. Simak, A. Udías, H.-K. Mao, and R. Ahuja, *Proc. Natl. Acad. Sci. USA* **107**, 9507 (2010).
- [104] B. Romanowicz, A. Cao, B. Godwal, R. Wenk, S. Ventosa, and R. Jeanloz, *Geophys. Res. Lett.* **43**, 93 (2016).
- [105] M. Ross, D. A. Young, and R. Grover, *J. Geophys. Res.: Solid Earth* **95**, 21713 (1990).
- [106] A. B. Belonoshko, R. Ahuja, and B. Johansson, *Nature (London)* **424**, 1032 (2003).
- [107] A. B. Belonoshko, N. V. Skorodumova, A. Rosengren, and B. Johansson, *Science* **319**, 797 (2008).
- [108] L. Vočadlo, I. G. Wood, M. J. Gillan, J. Brodholt, D. P. Dobson, G. D. Price, and D. Alfè, *Phys. Earth Planet. Inter.* **170**, 52 (2008).
- [109] A. B. Belonoshko, P. M. Derlet, A. S. Mikhaylushkin, S. I. Simak, O. Hellman, L. Burakovsky, D. C. Swift, and B. Johansson, *New J. Phys.* **11**, 093039 (2009).
- [110] A. B. Belonoshko, T. Lukinov, J. Fu, J. Zhao, S. Davis, and S. Simak, *Nat. Geosci.* **10**, 312 (2017).
- [111] S. Chatterjee, J. Ghosh, and T. Saha-Dasgupta, *Minerals* **11**, 258 (2021).
- [112] A. M. Dziewonski and D. L. Anderson, *Phys. Earth Planet. Inter.* **25**, 297 (1981).
- [113] E. Wasserman, L. Stixrude, and R. E. Cohen, *Phys. Rev. B* **53**, 8296 (1996).
- [114] M. Ekman, B. Sadigh, K. Einarsdotter, and P. Blaha, *Phys. Rev. B* **58**, 5296 (1998).
- [115] A. Laio, S. Bernard, G. L. Chiarotti, S. Scandolo, and E. Tosatti, *Science* **287**, 1027 (2000).
- [116] D. Alfè, G. D. Price, and M. J. Gillan, *Phys. Rev. B* **64**, 045123 (2001).
- [117] D. Alfè, G. D. Price, and M. J. Gillan, *Phys. Rev. B* **65**, 165118 (2002).
- [118] L. Koči, A. B. Belonoshko, and R. Ahuja, *Phys. Rev. B* **73**, 224113 (2006).
- [119] A. S. Mikhaylushkin, S. I. Simak, L. Dubrovinsky, B. J. N. Dubrovinskaia, and I. A. Abrikosov, *Phys. Rev. Lett.* **99**, 165505 (2007).
- [120] D. Alfè, *Phys. Rev. B* **79**, 060101(R) (2009).
- [121] C. J. Pickard and R. J. Needs, *J. Phys.: Condens. Matter* **21**, 452205 (2009).
- [122] E. Sola and D. Alfè, *Phys. Rev. Lett.* **103**, 078501 (2009).
- [123] X. Sha and R. E. Cohen, *Phys. Rev. B* **81**, 094105 (2010).
- [124] L. Stixrude, *Phys. Rev. Lett.* **108**, 055505 (2012).
- [125] J. Bouchet, S. Mazavet, G. Morard, F. Guyot, and R. Musella, *Phys. Rev. B* **87**, 094102 (2013).
- [126] D. A. Young, H. Cynn, P. Söderlind, and A. Landa, *J. Phys. Chem. Ref. Data* **45**, 043101 (2016).
- [127] T. Sun, J. P. Brodholt, Y. Li, and L. Vočadlo, *Phys. Rev. B* **98**, 224301 (2018).
- [128] D. C. Swift, T. Lockard, R. F. Smith, C. J. Wu, and L. X. Benedict, *Phys. Rev. Res.* **2**, 023034 (2020).
- [129] Z. Li, R. Caracas, and F. Soubiran, *Earth Planet. Sci. Lett.* **547**, 116463 (2020).
- [130] J. C. Boettger and D. C. Wallace, *Phys. Rev. B* **55**, 2840 (1997).
- [131] N. Tsujino, Y. Nishihara, Y. Nakajima, E. Takahashi, K. Funakoshi, and Y. Higo, *Earth Planet. Sci. Lett.* **375**, 244 (2013).
- [132] S. A. Dyachkov, D. K. Ilnitsky, A. N. Parshikov, and V. V. Zhakhovsky, *J. Phys.: Conf. Ser.* **1556**, 012032 (2020).
- [133] G. I. Kerley, *Multiphase Equation of State for Iron*, Tech. Rep. SAND93-0027, UC-410 (Sandia National Laboratories, 1993).
- [134] A. B. Medvedev, *Combust. Explos. Shock Waves* **50**, 582 (2014).
- [135] T. Sjostrom and S. Crockett, *Phys. Rev. E* **97**, 053209 (2018).
- [136] C. J. Wu, P. C. Myint, J. E. Pask, C. J. Prisbrey, A. A. Correa, P. Suryanarayana, and J. B. Varley, *J. Phys. Chem.* **125**, 1610 (2021).
- [137] D. A. Liberman, *Phys. Rev. B* **20**, 4981 (1979).
- [138] B. Wilson, V. Sonnad, P. Sterne, and W. Isaacs, *J. Quant. Spectrosc. Radiat. Transfer* **99**, 658 (2006).
- [139] D. C. Wallace, *Statistical Physics of Crystals and Liquids: A Guide to Highly Accurate Equations of State* (World Scientific, Singapore, 2003).
- [140] A. A. Correa, L. X. Benedict, D. A. Young, E. Schwegler, and S. A. Bonev, *Phys. Rev. B* **78**, 024101 (2008).
- [141] L. X. Benedict, T. Ogitsu, A. Trave, C. J. Wu, P. A. Sterne, and E. Schwegler, *Phys. Rev. B* **79**, 064106 (2009).
- [142] L. X. Benedict, K. P. Driver, S. Hamel, B. Militzer, T. Qi, A. A. Correa, A. Saul, and E. Schwegler, *Phys. Rev. B* **89**, 224109 (2014).

- [143] P. Vinet, J. H. Rose, J. Ferrante, and J. R. Smith, *J. Phys.: Condens. Matter* **1**, 1941 (1989).
- [144] W. B. Holzzapfel, *Rep. Prog. Phys.* **59**, 29 (1996).
- [145] D. A. Young and E. M. Corey, *J. Appl. Phys.* **78**, 3748 (1995).
- [146] M. G. Gorman, C. J. Wu, R. F. Smith, L. X. Benedict, C. J. Prisbrey, W. Schill, S. A. Bonev, R. W. Long, P. Söderlind, D. Braun, D. C. Swift, R. Briggs, T. J. Volz, E. F. O'Bannon, P. M. Celliers, D. E. Fratanduono, J. H. Eggert, S. J. Ali, and J. M. McNaney, *Phys. Rev. B* **107**, 014109 (2023).
- [147] P. Debye, *Ann. Phys.* **344**, 789 (1912).
- [148] This “fixed- ρ anharmonicity” is to be contrasted with the more basic phenomenon of θ being strongly ρ -dependent, which is of primary importance in the explanation of thermal expansion. The latter effect *is* included in our modeling [see Eqs. (2) and (4)]. Theories such as the one we employ (harmonic at each density, but with different vibrational spectra for different densities) for F_{ion} are termed “quasiharmonic” [155].
- [149] S. Zhang, B. Militzer, L. X. Benedict, F. Soubiran, P. A. Sterne, and K. P. Driver, *J. Chem. Phys.* **148**, 102318 (2018).
- [150] D. C. Swift, T. Lockard, R. G. Kraus, L. X. Benedict, P. A. Sterne, M. Bethkenhagen, S. Hamel, and B. I. Bennett, *Phys. Rev. E* **99**, 063210 (2019).
- [151] L. H. Thomas, *Math. Proc. Camb. Phil. Soc.* **23**, 542 (1927).
- [152] E. Fermi, *Endiconti: Atti Accad. Naz. Lincei* **6**, 602 (1927).
- [153] We note that the ϵ , γ , and δ phases of Fe are also believed to possess sizable local electronic spin moments; however, their spatial ordering is either far more subtle or nonexistent (depending on ρ and T) as compared to that of the α phase. It is for this reason that we do not include F_{mag} terms for these phases. Nevertheless, we stress that the presence of local magnetic moments does impact the *compressibility* of any phase that exhibits them; these effects are subsumed into our phase-dependent $F_{\text{cold}}(\rho)$ and $F_{\text{ion}}(\rho, T)$ terms for α , ϵ , γ , and δ , and are culled from our fitting to experimental data (see Sec. IV).
- [154] E. D. Chisolm and D. C. Wallace, *J. Phys.: Condens. Matter* **13**, R739 (2001).
- [155] E. D. Chisolm, S. D. Crockett, and D. C. Wallace, *Phys. Rev. B* **68**, 104103 (2003).
- [156] H. D. Whitley, D. M. Sanchez, S. Hamel, A. A. Correa, and L. X. Benedict, *Contrib. Plasma Phys.* **55**, 390 (2015).
- [157] A. A. Correa, L. X. Benedict, M. A. Morales, P. A. Sterne, J. I. Castor, and E. Schwegler, [arXiv:1806.01346](https://arxiv.org/abs/1806.01346).
- [158] Q. Xu, X. Jing, B. Zhang, J. E. Pask, and P. Suryanarayana, *J. Chem. Phys.* **156**, 094105 (2022).
- [159] L. Burakovsky and D. L. Preston, *J. Phys. Chem. Solids* **65**, 1581 (2004).
- [160] J. D. Van der Waals, *Over de Continuïteit Van Den Gas- En Vloeïstoftoestand* (University of Leiden, A. J. Sijthoff, Leiden, Netherlands, 1873), Vol. 1.
- [161] G. Kresse and J. Hafner, *Phys. Rev. B* **47**, 558(R) (1993).
- [162] G. Kresse and J. Hafner, *Phys. Rev. B* **49**, 14251 (1994).
- [163] G. Kresse and J. Furthmüller, *Comput. Mater. Sci.* **6**, 15 (1996).
- [164] G. Kresse and J. Furthmüller, *Phys. Rev. B* **54**, 11169 (1996).
- [165] J. P. Perdew, K. Burke, and M. Ernzerhof, *Phys. Rev. Lett.* **77**, 3865 (1996).
- [166] J. P. Perdew, K. Burke, and M. Ernzerhof, *Phys. Rev. Lett.* **78**, 1396 (1997).
- [167] P. E. Blöchl, *Phys. Rev. B* **50**, 17953 (1994).
- [168] G. Kresse and D. Joubert, *Phys. Rev. B* **59**, 1758 (1999).
- [169] S. Nosé, *J. Chem. Phys.* **81**, 511 (1984).
- [170] W. G. Hoover, *Phys. Rev. A* **31**, 1695 (1985).
- [171] See the Russian Academy of Sciences Shock Wave Database, <http://www.ihed.ras.ru/rusbank/>, and the references cited within.
- [172] Y. S. Touloukian, *Thermal Expansion: Metallic Elements and Alloys* (IFI/Plenum, New York, 1975).
- [173] S. Klotz, Y. L. Godec, T. Strässle, and U. Stuhr, *Appl. Phys. Lett.* **93**, 091904 (2008).
- [174] L. J. Swartzendruber, *Bull. Alloy Phase Diagrams* **3**, 161 (1982).
- [175] P. Söderlind (private communication).
- [176] M. T. Beason and B. J. Jensen, *Phys. Rev. B* **105**, 214107 (2022).
- [177] We use the shock (followed by shallow release) plus ramp compression stresses from columns 2, 3, and 4 of Table S2 in the Supplemental Material of Kraus *et al.* [85].
- [178] J. J. Gilvarry, *Phys. Rev.* **102**, 308 (1956).
- [179] R. M. Darlington, T. L. McAbee, and G. Rodrigue, *Comput. Phys. Commun.* **135**, 58 (2001).
- [180] V. A. Dobrev, T. V. Kolev, and R. N. Rieben, *SIAM J. Sci. Comput.* **34**, B606 (2012).
- [181] C. R. Noble, A. T. Anderson, N. R. Barton, J. A. Bramwell, A. Capps, M. H. Chang, J. J. Chou, D. M. Dawson, E. R. Diana, T. A. Dunn *et al.*, *ALE3D: An Arbitrary Lagrangian-Eulerian Multi-Physics Code*, Tech. Rep. LLNL-TR-732040 (Lawrence Livermore National Laboratory, Livermore, CA (United States), 2017).
- [182] W. W. Anderson and T. J. Ahrens, *J. Geophys. Res.: Solid Earth* **99**, 4273 (1994).
- [183] P. C. Myint, L. X. Benedict, C. J. Wu, and J. L. Belof, *ACS Omega* **6**, 13341 (2021).
- [184] D. J. Stevenson, *Annu. Rev. Earth Planet Sci.* **15**, 271 (1987).
- [185] W. B. Holzzapfel, *High Press. Res.* **30**, 372 (2010).
- [186] W. B. Holzzapfel, *High Press. Res.* **16**, 81 (1998).
- [187] F. N. Fritsch and R. E. Carlson, *BIMOND: Monotone Bivariate Interpolation Code (Preliminary Documentation)*, Tech. Rep. UCID-30197 (Lawrence Livermore National Laboratory, Livermore, CA, 1984).